Realistic morphological models of weakly to strongly branched pore networks for the computation of effective properties

Léo Moutin, Joane Meynard, Marc Josien, Michel Bornert, Christelle Duguay, Frédéric Adenot, Vincent Bouineau, Laurent Fayette, Renaud Masson

▶ **To cite this version:**

Léo Moutin, Joane Meynard, Marc Josien, Michel Bornert, Christelle Duguay, et al.. Realistic morphological models of weakly to strongly branched pore networks for the computation of effective properties. International Journal of Solids and Structures, 2023, 275, pp.112249. 10.1016/j.ijsolstr.2023.112249 . hal-04420651

HAL Id: hal-04420651
https://hal.science/hal-04420651v1

Submitted on 26 Jan 2024

HAL is a multi-disciplinary open access archive for the deposit and dissemination of scientific research documents, whether they are published or not. The documents may come from teaching and research institutions in France or abroad, or from public or private research centers.

L'archive ouverte pluridisciplinaire **HAL**, est destinée au dépôt et à la diffusion de documents scientifiques de niveau recherche, publiés ou non, émanant des établissements d'enseignement et de recherche français ou étrangers, des laboratoires publics ou privés.

International Journal of Solids and Structures 275 (2023) 112249

Contents lists available at ScienceDirect

International Journal of Solids and Structures

journal homepage: www.elsevier.com/locate/ijsolstr

Realistic morphological models of weakly to strongly branched pore networks for the computation of effective properties

Léo Moutin [a], Joane Meynard [a], Marc Josien [a], Michel Bornert [b], Christelle Duguay [a], Frédéric Adenot [a], Vincent Bouineau [a], Laurent Fayette [a], Renaud Masson [a,*]

[a] CEA, DES, IRESNE, DEC, Cadarache, F-13018 Saint-Paul-lez-Durance, France
[b] Laboratoire Navier, Ecole des ponts, Univ. Gustave Eiffel, CNRS, 6-8 avenue Blaise Pascal, Champs-sur-Marne, 77455 Marne-la-Vallée Cedex, France

ARTICLE INFO

Keywords:
Porous solids
Pore network
Inter-granules Porosity
Morphological descriptors
Virtual microstructures generation
Thermal conductivity
Homogenization
Representative volume element
FFT computation
UO_2 ceramics

ABSTRACT

We provide a detailed expository report of a new methodology aiming at building a numerical model of the complex pore distribution of porous UO_2 ceramics, tunable to real materials, in view of computing their effective thermal behavior. First, based on 2D optical microscopy images, we characterize the material of interest, dedicating a special attention to the porous network because of its major influence on the thermal behavior. Following Meynard et al. (2022), we then propose a simple morphological model combining a Voronoi tessellation and a boolean model, involving a limited number of parameters, from which 3D virtual microstructures (and so 2D cross-sections) can be generated. These parameters are tuned in order to select within our class of models the microstructures that are the most representative of the real ones ; in practice, this optimization process minimizes a cost function based on morphological descriptors computed from the 2D cross-sections. Last, we perform 2D full-field thermal simulations on cross-sections through Representative Volume Elements of both the numerical and the experimental microstructures. We validate our approach by qualitative and quantitative comparisons relative to both global properties and local field statistics.

1. Introduction

Knowledge of the physical behavior of solids is essential to predict the phenomena involved during their life of use. This behavior strongly depends on their microstructural characteristics. In particular, for porous solids, the pore geometry should be precisely characterized because it determines their physical properties and in particular their thermal and mechanical behaviors (Torquato and Haslach, 2002). The materials studied here are uranium dioxide (UO_2) ceramics obtained by sintering a powder of multi-crystalline granules. They differ from the standard UO_2 ceramics used in nuclear power plants as they could show a strongly extended porous network. The effect of porosity on the physical properties has already been studied extensively for standard UO_2 ceramics, but remains relatively unknown for the ceramics of interest. Initial work has been conducted to characterize this porosity. More precisely, it was shown in Meynard (2019) that pores observed in these ceramics are not randomly distributed all over the material since many of them are located at the interfaces between granules. For this reason, this latter part of the porous space is referred to as inter-granules porosity. By modeling this porosity by cracks, it was also shown that this particular spatial distribution of pores has an important influence on the thermal behavior of the considered porous solids (see Sevostianov and Kachanov, 2019; Meynard et al., 2022).

To characterize a material microstructure, it is necessary to observe it on a scale representative of the features constituting it. Many imaging methods allowing different perspectives can be used. One may distinguish methods giving access to cross-sectional images (2D imaging) such as the optical microscopy (Remy et al., 2014) and methods giving access to volumetric images (3D imaging) such as the Focus Ion Beam Scanning Electron Microscopy (FIB-SEM, Dowek et al., 2021) or the X-ray computed tomography (Salvo et al., 2003). We study here 2D sections of the ceramics of interest obtained by optical microscopy as it gives access to large domains which provide a statistically representative description of the microstructure. It would not be the case for FIB-SEM acquisitions which are limited in size neither for X-ray tomography acquisitions that remains also limited in volume for very dense materials like UO_2 (10.96 g/cm^3) because X-ray transmission is very low.

Mathematical morphology is a discipline of image processing initiated by Matheron (1967) and Serra (1982) which is based on the use of structuring elements to define morphological properties of objects.

* Corresponding author.
E-mail address: renaud.masson@cea.fr (R. Masson).

https://doi.org/10.1016/j.ijsolstr.2023.112249
Received 7 December 2022; Received in revised form 15 March 2023; Accepted 3 April 2023
Available online 13 April 2023
0020-7683/© 2023 Elsevier Ltd. All rights reserved.

In Coster and Chermant (1989), a method is introduced to reduce objects to their skeletons (i.e. a one pixel wide representation of each object which preserves its extent, orientation, and connectivity). This method is valuable in our case as it allows to associate the porous network to a crack network, thus highlighting its first order impact on the thermal behavior of ceramics and simplifying its description. Different tools can then be used to characterize such crack network. The length of the intercepts (Abrams, 1971) is used to assess the density and the orientation of the network while Matheron's granulometry (Matheron, 1967) provides a methodology to characterize the size distribution of inter-porous spaces. By extracting relevant information, a geometrical description of the microstructure of the studied ceramics can be obtained.

In some cases it is impossible to obtain data, especially in 3D, on a real material either because the experimental techniques do not allow it or because the material is too expensive to handle or to manufacture. It may then be interesting to use a virtual material. In this case, it is necessary to develop a virtual microstructure model that is as representative as possible of the real material. A major principle in the study of heterogeneous materials is the reduction of the study volume to a representative volume element (RVE) which is the smallest volume that is statistically representative of the material properties. Thus, a way of studying heterogeneous materials is to reproduce numerically, as accurately as possible, a RVE (Kanit et al., 2003) of their microstructure. These virtual RVE are then used to calculate effective properties such as the thermal conductivity or elastic moduli by full-field simulations.

An overview of possible methodologies to generate virtual microstructures is presented in Bargmann et al. (2018). The first of the three main families of microstructure generation methods identified by these authors is based on direct reconstruction of the microstructure from experimental images. The second one is based on the simulation of the manufacturing process of the material. The third and last method, which is the one adopted in this work, is based on the use of probabilistic approaches to generate random microstructures like a dispersion of particles (stochastic point processes), granular structures (random tessellations of space), etc. The development of these generation methods was notably led by Jeulin (2000). These methods are still motivating new works as for example Neumann et al. (2020) who tested the response of random virtual microstructures generated using the graph-based models of random structures introduced in Gaiselmann et al. (2014) or Gasnier et al. (2018b) who simulated the effective elastic behavior of virtual microstructures obtained by cracking some grain facets of a Johnson–Mehl tessellation. Using the same probabilistic methodology, a first model of the thermal barriers affecting the UO_2 ceramics under consideration was derived in Meynard et al. (2022) by superimposing a Voronoi tessellation modeling the inter-granules network with a random dispersion of overlapping spheres. Various random microstructures with porosities located at the interfaces between granules were generated in this way and rather wide ranges of effective thermal properties were computed for similar overall porosity levels, showing the strong influence of the pore morphology for such materials. The challenge is now to specify how the parameters used to generate such microstructures need to be chosen to obtain realistic virtual microstructures and, more precisely, to quantify how representative of the real ceramics of interest these virtual microstructures can be, in order to optimize this choice of parameters.

Altendorf et al. (2014) addressed this question of generating virtual microstructures that are as representative as possible of real ones by determining key material properties (fiber curvature, orientation and distribution) from 3D tomography images. These key material properties were then used as input parameters of the virtual reconstruction. In Hsu et al. (2021), a learning algorithm is developed to generate random microstructures that are topologically close to microstructures from a database made up of 3D Xe Plasma FIB-SEM images. Here, we make use of a more direct approach based on an automatic optimization of the parameters of the generation method introduced in Meynard et al. (2022). This optimization relies on the characterization of 2D cross-sections of the ceramics of interest obtained by optical microscopy to extract some characteristics of the porous network (orientation, density, size distribution of inter-porous space) and generates virtual microstructures that mimic these characteristics.

The objective of this work is to model 3D microstructures from 2D cross-sectional images in order to simulate their effective 3D properties, especially their effective conductivity. The paper is organized as follows. In Section 2, we present the studied UO_2 ceramics as well as the image acquisition and processing methods developed to characterize their microstructures. In particular, we introduce a laboratory-made code developed to evaluate the length of skeletonized objects (Abrams, 1971), named *Crackcut*. We then recall, in Section 3, the main lines of the method of generation of microstructures proposed by Meynard et al. (2022) and introduce the new optimization process. Finally, in Section 4, we propose an original way to evaluate the ability of the generated virtual microstructures to reproduce faithfully effective thermal properties by simulating the thermal behavior of cross-sections of these microstructures, on the one hand, and the processed optical microscopy images of the cross-sections of the real studied materials on the other hand, and by comparing the results in detail. The Fast Fourier Transform (FFT) method initially proposed by Moulinec and Suquet (1998) and widely used to simulate the thermal and mechanical behavior of various materials (Altendorf et al., 2014; Bluthé et al., 2021) is adopted to perform these simulations.

2. Studied material description and characterization

We consider in this study uranium dioxide ceramics whose porous network varies noticeably according to the manufacturing conditions. This porous network is made up of inter-granules pores as stated in the introduction but also of intra-granules pores which can be highlighted at a much smaller scale. We focus here on the inter-granules pore network as it plays at the first order on the degradation of the thermal conductivity. Even though the proposed characterization method is applied here to a particular material, it is however general and applicable to many other situations and materials in which a porous network of the type considered here is found, for example an inter-granular porous network in metals.

2.1. Material

Uranium dioxide is the usual fuel used in nuclear pressurized-water reactors. This ceramic material is manufactured using a standard powder metallurgy dry-route process (Delafosse and Lestiboudois, 1976; Bailly et al., 1996) which involves different steps including:

- A pre-compaction operation (at a pressure P_{prec}) followed by a granulation stage that are performed to increase the flowability of the UO_2 powder.
- A shaping step performed by uniaxial die pressing (at a pressure P_{press}).
- A sintering stage that allows to consolidate the obtained materials and reach the required density.

In this protocol, the pre-compaction pressure is lower than the pressing pressure ($P_{prec} < P_{press}$). In the prospect of investigating the influence of the porous network on the thermal behavior of UO_2 ceramics, an alternative process is considered in this article in which the pre-compaction pressure is higher than the pressing pressure ($P_{prec} > P_{press}$) (François and Gremeret, 1968). This alternative process favors the formation of an extended inter-granules porous network in the obtained UO_2 ceramics (Meynard, 2019).

Several ceramics were manufactured with this alternative process in order to characterize this inter-granules porosity and to evaluate its influence on the thermal behavior of the ceramics. The manufacturing conditions were tuned to obtain samples over a wide range of porosity.

Table 1
Volume fraction of open porosity (c_o) related to the studied ceramics.

Ceramics	C_1	C_2	C_3	C_{3*}
c_o (%)	0.9	1.1	3.45	3.45

Among these samples, four were selected to cover the considered porosity range. These samples are called "reference ceramics" hereafter by opposition to the virtual ones considered later.

The open porosity of each reference ceramic was experimentally measured by immersion in a wetting liquid (Pinot, 2015); here the bromobenzene liquid was used. Due to their slender shape, interconnections of inter-granules pores in the volume are expected and therefore, the open porosity is roughly well correlated with the inter-granules porosity. The reference ceramics are denoted C_k with $k \in \{1; 2; 3; 3^*\}$ in the following and are ordered from the lowest to the highest open porosity volume fraction (Table 1). Ceramics C_3 and C_{3*} have the same open porosity volume fraction but their inter-granules porosities and thermal behaviors differ as explained in next sections.

To evaluate the characteristics of the inter-granules porous network, optical microscopy images were acquired on these ceramics. Details on the image acquisition and processing method are given in the next section.

2.2. Image acquisition and processing methods

Images of cross-sections of the studied ceramics were captured by optical microscopy. This technique provides 2D images from which a quantitative characterization of the porous network of ceramics can be performed. One of its main advantages is the relative simplicity to capture images (as opposed to other methods of image acquisition, particularly in 3D) which makes it possible to study a large number of microstructures. However, the 2D nature of the obtained images induces the loss of the 3D features of the porous network.

The preparation of the samples consists of a cutting step with a wire saw and a polishing of the surface. The cuts are made through a plane parallel to the pressing direction. In the following sections, the horizontal axis of the obtained images is referred to as the x axis and the vertical axis, which is parallel to the direction of the uniaxial die pressing, as the y one. The protocol was optimized to limit as much as possible the UO_2 grains pulling out during the sample preparation (which could bias the characterization performed afterwards) in particular by resin-impregnating with an Epoxy resin the ceramics prior to cutting. The acquisition of images was carried out with an Olympus DSX500 opto-numerical microscope equipped with a CCD color camera with an image definition of 1688×1248 pix^2. Large regions of interest (ROIs) of the materials can be imaged by means of the automatic stitching of several images produced by the digital camera: more precisely 8 images along the x direction have been combined to produce one large image.

We used the same acquisition and lighting conditions for all images to ensure reliable comparisons between samples. The optical magnification was about 3x with a numerical aperture of the objective lens, reference MPLFLN5XBDP, of 0.15, resulting in physical pixel size of 1.52 μm/pixel. Illustrative views of local areas of the investigated ROIs are presented in Fig. 1 for the four considered materials.

It clearly appears that when the volume fraction of the open porosity increases, the amount of inter-granules pores observed on the optical images increases as well. More precisely, the inter-granules pores seem to be more extended and branched. Also, even if C_3 and C_{3*} present the same open porosity volume fraction, the observed inter-granules pores show clearly different features. Indeed, compared to C_3, the porous network of C_{3*} seems to show a more pronounced preferred orientation along the horizontal axis (in the optical microscopy images) which would result from the pressing step carried out during the manufacturing process.

Once the image acquisition is done on a given microstructure, several processing steps are necessary to clearly isolate the objects of interest that are, in our case, the inter-granules pores. Our image processing protocol consists of four main operations, to go from a raw image obtained by optical microscopy to a skeletonized image. The skeletonization allows a simple description of the porous network as a network of "cracks", i.e. objects with no thickness, described by one-pixel-wide lines in binary images. It also allows us, by neglecting the porosity thickness, to limit the impact of the potential pullouts produced during the preparation of the samples. The four steps of our protocol, illustrated in Fig. 2, are the following:

- A thresholding of the 8-bit grayscale images (on which 0 corresponds to black and 255 to white) to binarize the images (Burger and Burge, 2008). The threshold value is set to $S = H_{mean} - 27$ where H_{mean} represents the average grayscale intensity over the whole image and S is such as the pixels below this value are labeled black and the ones above are labeled white. This threshold value was chosen as it provides an appropriate separation between the matrix and the inter-granules porosity based on their intensities on the gray-scale histogram.[1] After this step, the black objects in the image depict the inter-granules porosity. Note that, since the acquisition conditions are identical for all the images and the pore volume fractions are low (< 5 %), we have very low gray level fluctuations from one image to another. Using a threshold depending on the considered image (through H_{mean}) rather than a fixed threshold allows nevertheless to get rid of possible small variations in images brightness.
- An elimination of objects which are not inter-granules pores, such as surface defects related to the polishing process, image artifacts or elements on the ceramic microstructure present at a scale lower than the one of the inter-granules porosity, including in particular smaller intra-granules pores. To do so, we remove from the images the connected components that have a circularity[2] higher than $R_{circ} = 0.4$ as they do not present the slender shape characteristic of the inter-granules porosity. This value was found to offer the best compromise between the elimination of unwanted objects and the preservation of inter-granules pores. This step allows us to keep only the crack-like type objects which are associated with the inter-granules porosity.
- A morphological closing of the remaining slender enough objects in the resulting binary image with a disk of radius $r = 5$ pixels acting as the structuring element.[3] This pre-processing is necessary to smooth out the roughness of elements on the binarized image and thus guarantees a skeletonization giving a representative image of the inter-granules porosity. The morphological closing is obtained by a dilation followed by an erosion with the same structuring element. The radius of the disk was chosen after a study of the influence of this parameter on the ultimately obtained skeletonized image, $r = 5$ having proven to provide the best result in terms of keeping the porosity shape and connectivity. Beyond this practical point of view, it should be emphasized that the choice of this size of structuring elements introduces a length scale into the proposed image processing. This length is the one at which the inter-granules pores act as local thermal barriers at the granules scales. Smaller details relative to the structure of inter-granules

[1] Alternative methods as the one proposed by Otsu (1979) have been tried but remain poorly adapted to the slender objects considered here.

[2] Ratio of the area of an object to that of a circle of equivalent diameter. We evaluate the circularity with the Analyze Particles function of ImageJ. The formula to calculate the circularity is $R_{circ} = 4\pi \frac{area}{perimeter^2}$ which gives $R_{circ} = 1$ when applied to a perfect circular object.

[3] The morpholibJ plug-in is used for this operation (Legland et al., 2016)

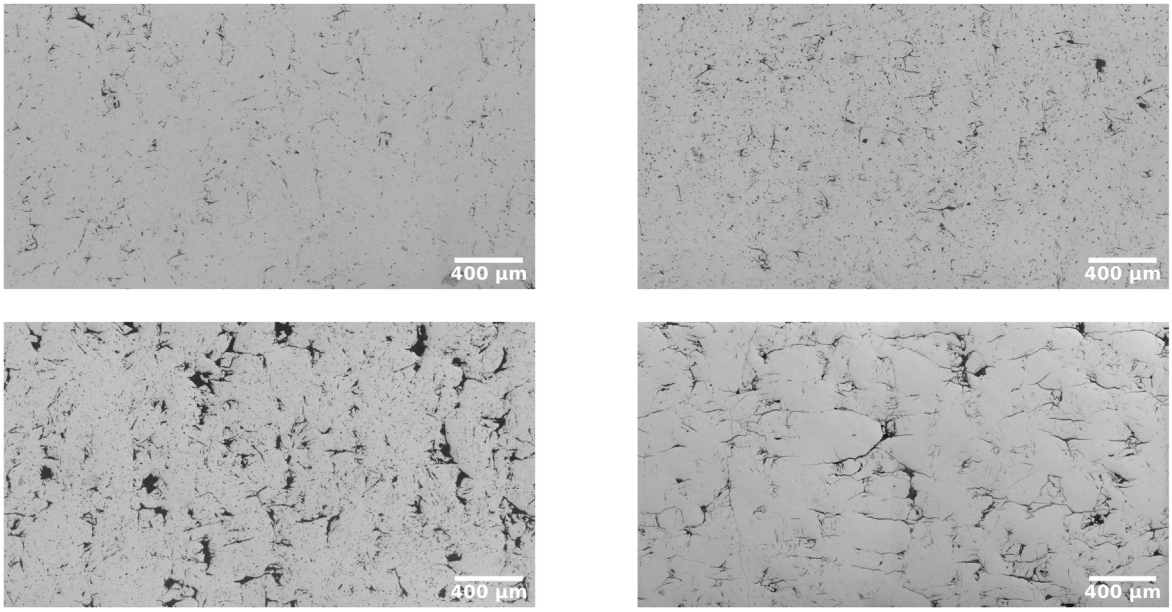

Fig. 1. Enlarged views (2048 × 1100 pix^2, i.e areas of about 3.1x1.7 mm^2)) on the raw optical microscopy images obtained on the reference ceramics: C_1 (top left), C_2 (top right), C_3 (bottom left) and C_{3^*} (bottom right).

Fig. 2. Illustrations of the four processing operations used to transform a raw image of the reference ceramics obtained by optical microscopy into a skeletonized image of their inter-granules porosity. From left to right: initial image, thresholding, elimination of unwanted objects based on the circularity of connected components in the binary image, smoothing of the edges of the pores by a morphological closing of appropriate size and skeletonization of the resulting objects.

pores are unnecessary to describe their effects at granule scale, while smoothing over a larger scale might have hidden some local phenomena within grains.

– And finally, the skeletonization of the image can be processed, that is to say the reduction of the thickness of the objects to 1 pixel (Coster and Chermant, 1989). In the following, the skeletonized inter-granules pores will be referred to as "cracks".

The obtained skeletons provide a concise description of the inter-granules pores observed on the raw optical images in terms of extent, orientation and connectivity (Fig. 2). Thus, the use of the skeletonized images is of interest in this study since the topological "skeleton" encodes the main geometrical features of the porous network. From these images, it is possible to extract different quantities that are significant of the state of the inter-granules porous network. The left column of Fig. 3 shows the skeletonized images obtained from the different reference ceramics. For the sake of readability of the images, the skeletons have been dilated with a diamond-shaped structuring element of 2 pixels. The skeletonized images confirm that the inter-granules pores become more extended and branched as the volume fraction of the open porosity increases.

2.3. Microstructural characterization

We seek here to statistically describe the microstructure of the reference ceramics. Five descriptors were selected to quantify the density of the network, the spatial distribution of cracks and their lengths.

2.3.1. Pore network density, anisotropy and interpore size distribution

We are primarily looking to characterize the density of the crack network of the ceramics by evaluating how extended it is. For this purpose, the first selected descriptor is the length of the intercepts (Abrams, 1971; Thompson, 1972). It quantifies the spacing between two cracks in a given direction based on the number of cracks intersected by a line of specified length and orientation. For an isotropic microstructure, any direction can be chosen for the line. Hence, we quantify the density of the crack network by calculating the statistical distribution of the intercept lengths along x.

We can note that, since this quantity depends on the orientation of the drawn lines, by choosing well this orientation it allows us to account for the possible anisotropy of the studied microstructures. Although this dependency should ideally be fully explored by testing all orientations, in our case the approach can be simplified by simply comparing the results along x and y since the manufacturing process is symmetrical with respect to these two directions (notably because P_{prec} and P_{press} are imposed along y). Thus, we evaluate the anisotropy of C_{3^*} by studying the statistical distribution of the ratio of the intercept lengths along x and y. The precise quantity considered to quantify this anisotropy will be defined later. In the case of an isotropic ceramic (random orientation of cracks) the intercept lengths along x and along y are equal and the ratio then tends towards 1.

Another feature which provides interesting information on the state of the crack network is the size distribution of inter-porous spaces. To assess the latter, we use a quantity that is based on the principles of Matheron's granulometry (Matheron, 1967). G. Matheron laid the

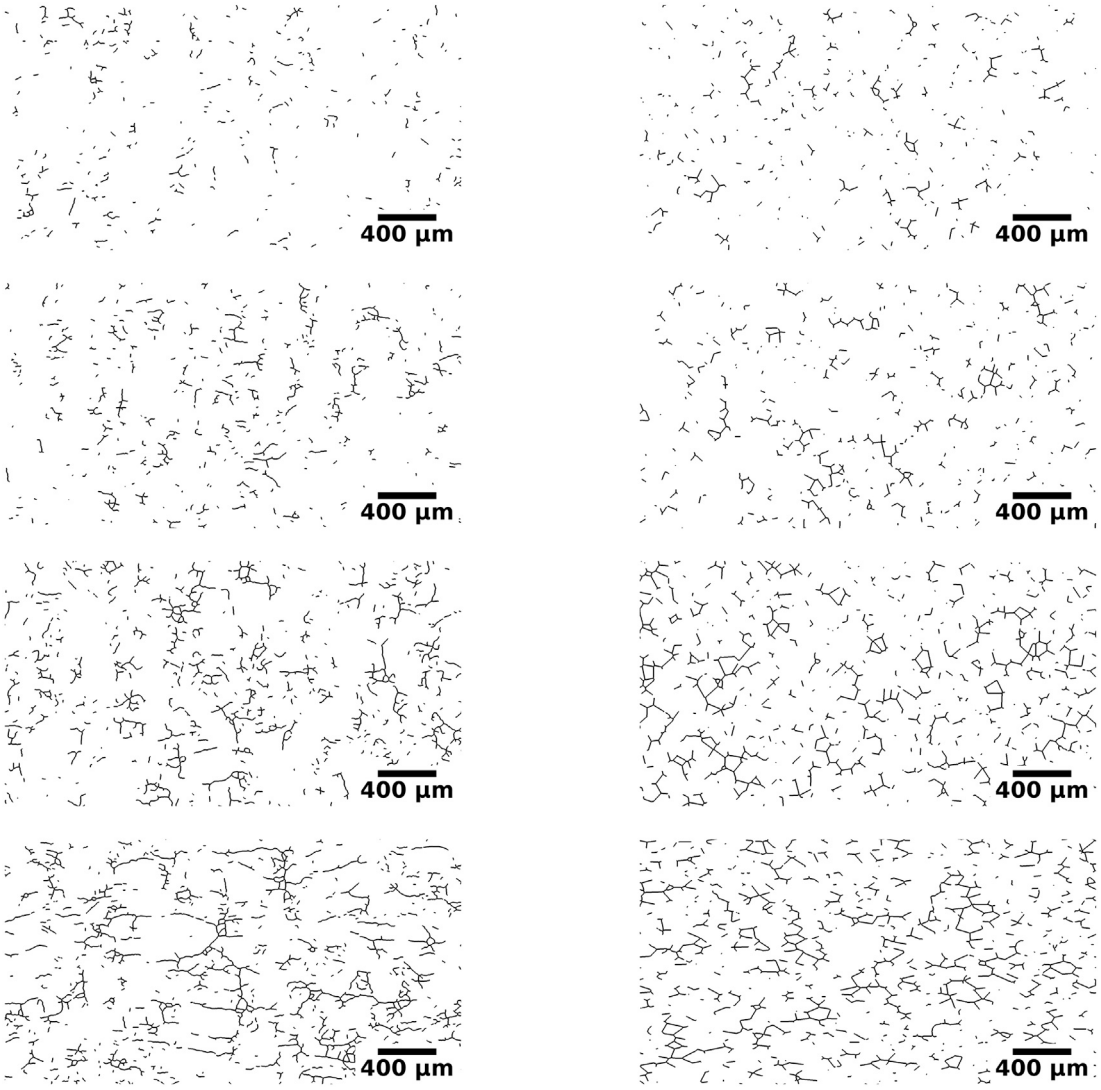

Fig. 3. Enlarged views (2048x1100 pix^2) on the skeletonized images of the reference microstructures (left column) and of the tuned microstructures (right column, see part 3.2.3). From top to bottom: C_1, C_2, C_3 and C_{3^*}. The pixel size is 1.52 µm/pixel.

foundations of mathematical morphology and in particular introduced the concept of size using openings[4] by convex structuring elements to evaluate the size distribution of objects present in a binarized image. In our case, the structuring element considered is the simplest possible, i.e. the circle, since it does not introduce any anisotropy. Thus, we characterize the spatial distribution of cracks by evaluating the size distribution of the radius of the largest circles that can be inserted between the cracks.

2.3.2. Crack length

The crack length is also an important characteristic as it gives an idea of the extent of the thermal barriers present in the material. However, as it can be seen in Fig. 3, pores are interconnected and thus the definition of their length (based on their skeletons) is not straightforward. Therefore, we chose to evaluate the length of the porous network by estimating two quantities that are more easily accessible, namely the lengths of the branches (l_{bra}) and of the primary branches ($l_{braPrim}$) of the skeletons. By convention, we call "branches" the objects obtained after having eliminated the nodes where the branches of the skeleton meet (referred as connection points) and "primary branches" the objects obtained by holding the geodesic diameter of the cracks. The geodesic diameter is by definition the length of the longest geodesic path that it is possible to travel within a particle (Lantuejoul and Maisonneuve, 1984; Makai, 1973; Morard et al., 2011). The length of the primary branches allows us to account for the first-order impact of cracks on the thermal conductivity of the microstructure since the primary branches represent the main barriers for the heat flux. The length of the branches has a lesser impact on the thermal properties, but the ratio between length of primary branches and branches provides a measurement of the branching of cracks. Indeed, for a very ramified microstructure, the length of the primary branches will be significantly larger than that of the branches. An imageJ plugin, called *Crackcut*, has been developed in Meynard (2019) to extract key parameters from a skeletonized image and in particular to assess the length of branches and primary branches. This calculation code allows to obtain, from a skeletonized image, the branches (by eliminating the connection points) and the primary branches (by evaluating the geodesic diameters) and then to calculate the length of the rectilinear objects present on the processed image (see Appendix A).

A bias can be introduced by the objects (branches and primary branches) that intersect the edges of the image and that are therefore cut off. It was then verified, for the different studied microstructures, that there was no significant evolution of the cumulative distribution

[4] Opening = an erosion followed by a dilation

on the size of the branches and primary branches in the case when the objects on the edges are counted and when they are not considered (lower than 5 %). The boundary effects are low particularly because the considered images are large enough in comparison to the size of the objects of interest.

In what follows, for the different selected quantities, we will systematically study the cumulative distributions.[5] Cumulative distributions are defined by the variable H_Q with Q representing the different quantities presented above. Our magnitudes of interest are then $H_{Intercepts}$, $H_{Intercepts,x}/H_{Intercepts,y}$, $H_{Matheron}$, H_{branch} and $H_{PrimaryBranch}$. The quantity used to evaluate the anisotropy of a microstructure corresponds precisely to the ratio of the cumulative distribution functions of intercept lengths along x and y at the same distance ($H_{Intercepts,x}/H_{Intercepts,y}$). For the sake of simplicity, it will be called hereafter "ratio of the intercepts".

All the different quantities presented above are used in Section 2.3.4 to characterize the microstructures of the reference ceramics.

2.3.3. Ergodicity of experimental images

To ensure that the size of the images from which the characterization is performed is sufficient so that the measured quantities are representative, we relied on the asymptotic behavior method (Bruchon et al., 2013). We randomly drew $N_w = 100$ windows of fixed size (L_{2D}) in our images and we measured for each window the average length of the primary branches while gradually increasing L_{2D}. Fig. 4 shows the evolution of the relative standard deviation on the mean length of the primary branches ($\frac{\sqrt{Var(\langle l_{braPrim}\rangle_{L_{2D}})}}{\langle\langle l_{braPrim}\rangle_{L_{2D}}\rangle_{N_w}}$) where $\langle.\rangle$ and Var correspond respectively to the average and variance operator) as a function of L_{2D}. Since the size of the complete images is not infinite, it is not possible to ensure a random draw of independent elements as L_{2D} may become close to this size of the complete images. We have thus limited L_{2D} to 500 pixels, which is much smaller than the size of our images, to preserve the independence of the draws as well as possible. We chose to study the length of the primary branches because it is the least stable of the 5 variables as it is used to characterized large scattered objects.

We can see that the different ceramics have a rather close behavior. The relative standard deviation decreases linearly with L_{2D} in a log–log scale which means that the evolution trend is of the type $\frac{\sqrt{Var(\langle l_{braPrim}\rangle_{L_{2D}})}}{\langle\langle l_{braPrim}\rangle_{L_{2D}}\rangle_{N_w}} = A\ L_{2D}^{-b}$. To have a global evolution for all the ceramics we have averaged the different parameters (A and b) obtained for each ceramic. We can thus estimate the standard deviation for a window size of about 3000x3000 pix^2 (which is close to the size of the complete images from which we measure the characteristic quantities). We obtain with this method, for $L_{2D} = 3000$ pix, $\frac{\sqrt{Var(\langle l_{braPrim}\rangle_{L_{2D}})}}{\langle\langle l_{braPrim}\rangle_{L_{2D}}\rangle_{N_w}} = 0.015$. Therefore, little variability is observed for the magnitude studied at this image size ensuring thus the representativity of the measured quantities on the studied images for the characterized reference ceramics.

2.3.4. Results

To compare the characteristics of the microstructures of the reference ceramics, the cumulative distributions obtained with the different characterization quantities are plotted in Fig. 5. The slope of the cumulative distributions of the intercept lengths ($H_{Intercepts}$) increases with the concentration of cracks in the ceramics which is consistent since the average distance between two cracks naturally decreases when the linear density of cracks increases. This translates into a higher proportion of small intercept values and therefore a higher slope for the cumulative distribution. Furthermore, as we find largest intercepts when the concentration of cracks decreases, the width of the distribution increases at the same time. Similar comments can be made for the radius of 2D circles Matheron's granulometry. One could notice that the radius of Matheron's 2D granulometry are much lower than the length of the intercepts (10×) as they reflect the size of circular objects, not linear, which are more constrained by the presence of cracks around.

[5] Note that the cumulative distribution is more convenient than the distribution function to future optimization as it is more regular.

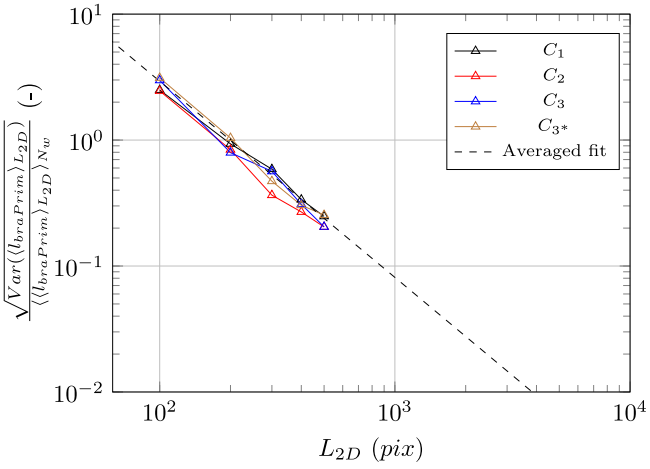

Fig. 4. Evolution of the relative standard deviation of the average length of the primary branches ($\frac{\sqrt{Var(\langle l_{braPrim}\rangle_{L_{2D}})}}{\langle\langle l_{braPrim}\rangle_{L_{2D}}\rangle_{N_w}}$) as a function of the size of the observed image. The pixel size is 1.52 µm/pixel.

An opposite behavior is observed for the length of the primary branches. Indeed, the geodesic diameter increases with the linear density of cracks since the interconnections between cracks become more frequent. A similar evolution, although much less marked, is observed regarding the lengths of the branches, which are much more similar in the various considered materials. Actually this quantity is more related to the grain size, which is expected to be similar because materials result from the same powder. It can be noticed that the ceramics C_3 and C_{3^*} have very similar characteristics and that these ceramics can be clearly discriminated only by taking into account the orientations of the cracks by means of the ratio of the intercepts. Considering the intercepts ratios in the two directions ($H_{Intercepts,x}/H_{Intercepts,y}$) in Fig. 5, it can also be noticed that the ceramics C_1, C_2, and to a lesser extent C_3, deviate from isotropy for small intercept lengths ($l_{intercepts} < 250$ pix). The choice to consider these ceramics as isotropic is justified by the fact that this anisotropy, which is restricted to small values of intercept lengths, has no effect on their thermal behavior, as it has been verified in Section 4.2.

Now that the reference ceramics as well as the tools used to characterize their microstructures have been introduced, we present in Section 3 the method of generating representative virtual microstructures (referred to as tuned microstructures in the following). We will also make use of the same above presented tools to characterize these virtual microstructures and to compare them to the reference ones.

3. Numerical generation of representative virtual microstructures

We aim at generating tuned microstructures that emulate the porous network of reference ceramics. As explained in the introduction, a model has been proposed in Meynard et al. (2022) to generate virtual microstructures with a crack network distributed at the interfaces between granules. As this method allows us to generate very different microstructures by varying the input parameters, we propose here a method to tune these parameters in order to simulate a given ceramic. This method relies on an automated optimization procedure that aims at producing a tuned microstructure, of which the quantities defined in Section 2.3 are as close as possible to their counterparts for the given ceramic.

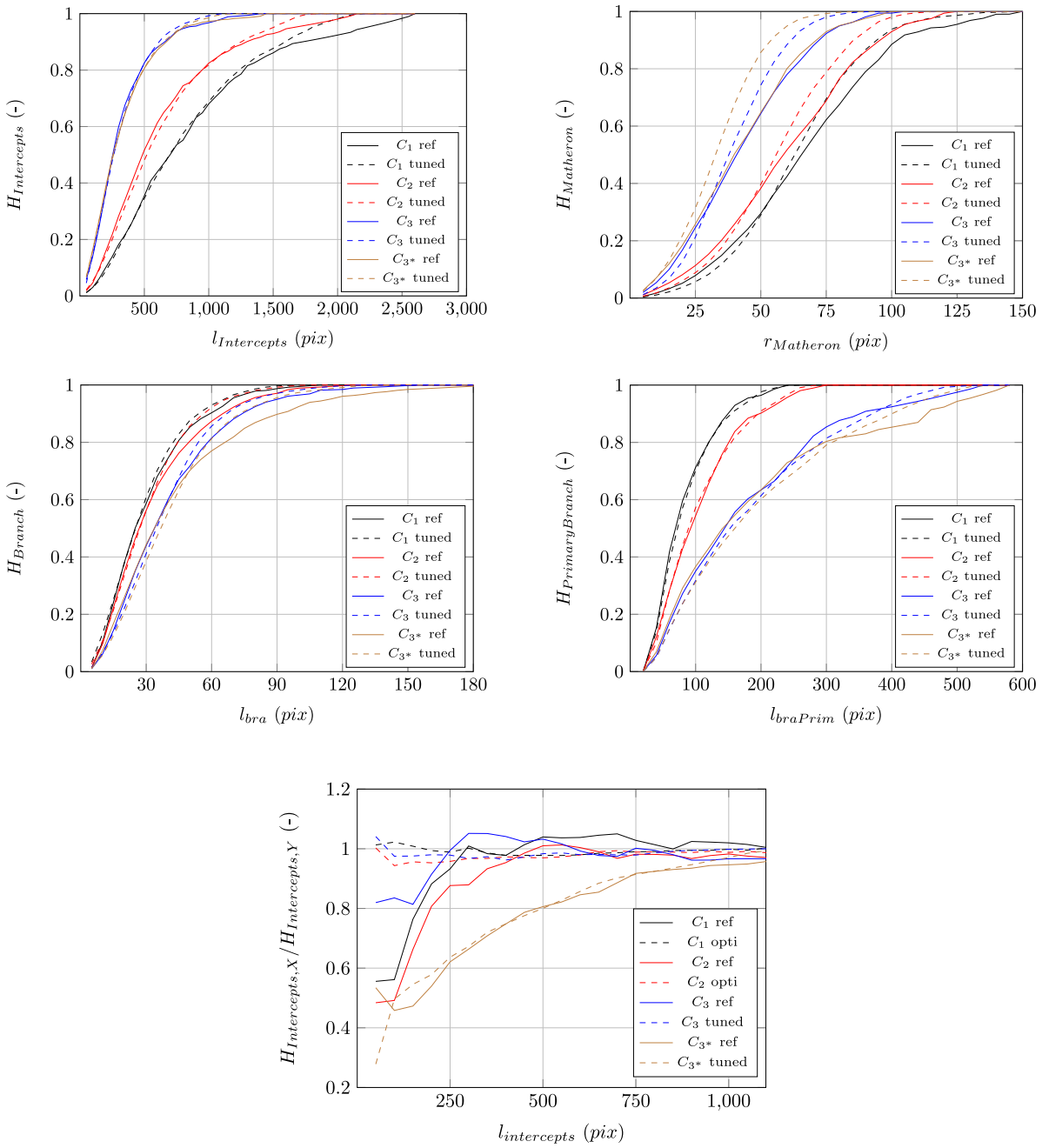

Fig. 5. Cumulative distributions associated with each characterization parameter obtained on the reference ceramics and on the tuned microstructures (see part 3.2.3). The pixel size is 1.52 µm/pixel.

3.1. Generation of virtual microstructures with a crack network located at the inter-granules boundaries

3.1.1. General method

The generation of virtual microstructures with a crack network located at the inter-granules boundaries (IGB) is achieved by combining two random sets (see Fig. 7 in this document and figure 3 in Meynard et al., 2022). The first set corresponds to the IGB and is obtained by generating a Voronoi tessellation with seeds that are distributed quasi-homogeneously using a RSA algorithm (Feder, 1980; Torquato et al., 2006; Ebeida et al., 2012). The input parameters for the drawing of seeds are the number of cells N_c and the dimension L of the periodic RVE. Using these two parameters and assuming that the seeds are perfectly homogeneously distributed in the RVE, we can approximate the radius of the non-intersecting spheres drawn from the seeds (which we assimilate to the average radius of the granules, denoted R_g):

$$R_g^3 = \frac{L^3}{\frac{4}{3}\pi\, N_c/0.384} \tag{1}$$

where the 0.384 value represents the maximum coverage rate that can be achieved using a 3-D RSA algorithm (see Table II in Zhang and Torquato, 2013).

Once the seeds are drawn, the Voronoi tessellation can be generated. The Voronoi criterion that defines the tessellation is $x \in G_i \Leftrightarrow \|x - c_i\| \leq \|x - c_n\| \ \forall n \in \{1, \dots, N_c\}$ (with $\|\cdot\|$ the Euclidean norm on the periodic cube) where x defines any point of the RVE and G_i defines the cell i of center c_i for $i \in [1, N_c]$. A quantity which allows to define the density of the IGB has been introduced in Meynard et al. (2022). This quantity, denoted A_V^{IGB}, is its area per unit of volume and depends directly on R_g. Indeed, it is shown in Meynard et al.

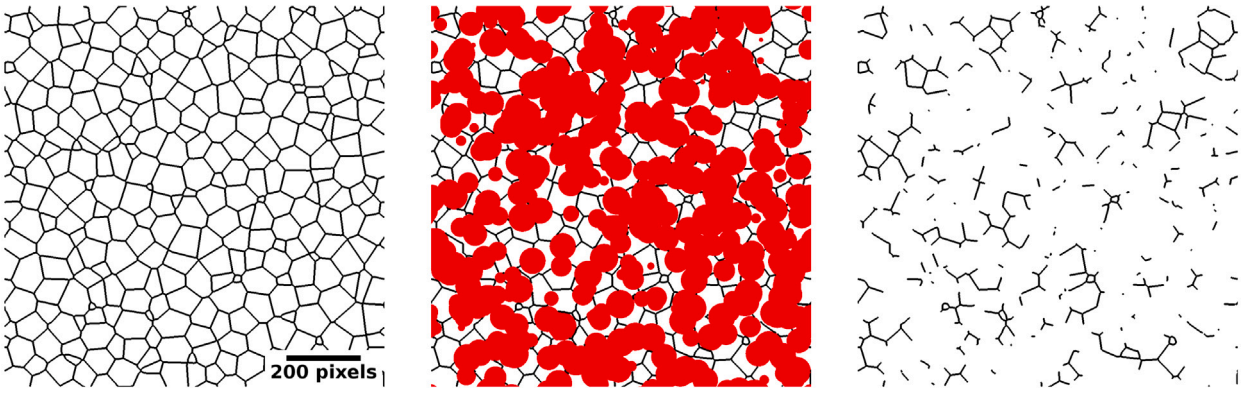

Fig. 6. 2D illustration of the steps in the 3D generation of a virtual microstructure with inter-granules porosity. From left to right: inter-granules porous network covering the whole inter-granules boundary, superimposed with a dispersion of delimiting spheres (middle figure) and the final cracked microstructure obtained by elimination of the intersection between the delimiting spheres and the porous network.

(2022) that, in the case of a Voronoi tessellation generated with a RSA process, $A_V^{IGB} \approx 1.26/R_g$. Using a Voronoi tessellation with quasi-homogeneously distributed seeds limits the number of input parameters needed for generating the IGB which is suitable for the following optimization that is described in Section 3.2. Of course, alternative methods exist for the tessellation and the consequences of the choices made on the obtained virtual microstructures will be discussed below, at the end of Section 3.2.

The second random set is obtained by generating a number N_l of spheres (called delimiting spheres), of radius R_l, randomly in the domain using a standard Poisson process, providing a Boolean model of spheres (Matheron, 1967).

The virtual microstructure with inter-granules porosity is finally obtained by eliminating the intersection between the first random set (IGB) and the second one (delimiting spheres). We underline that the generated RVE is periodic: if a crack or a sphere intersects a boundary of the RVE, it is duplicated on the opposite face. Periodicity is imposed for practical reasons, and in particular to be in agreement with the boundary conditions imposed in the thermal computations. Also, it must be specified that the model is first simulated in the Euclidean space and then intersected by the grid of points to generate images.

The Fig. 6 illustrates the different steps of the method of generation. The dispersion that can be observed in the size of the disks and granules is due to the fact that we observe a 2D section of a 3D generated microstructure.

This method has three input parameters which are R_g, R_l and d_l (the density of delimiting spheres, $d_l = (4/3)\,\pi\, N_l\,(R_l/L)^3$). By varying these three parameters, it is possible to obtain significantly different microstructures. As an example, it has been shown that it is possible in an extreme case ($R_g \gg R_l$) to obtain microstructures with cracks of the same size homogeneously distributed at the IGB and, in another one ($R_g \ll R_l$), microstructures with cracks located in preferential areas (clusters) (figure 6 in Meynard et al., 2022). This last point underlines the particularity of the developed model and it is what differentiates it from the approach followed in Gasnier et al. (2018b) in which the cracks are obtained by cracking some randomly chosen grain facets of a Johnson–Mehl tessellation.

3.1.2. Generation of oriented virtual microstructures

Various methods exist to generate objects with a preferred orientation (Falco et al., 2014; Mortazavi et al., 2015; Pérez et al., 2019). The idea that we retained here is to play directly on the shape of the granules by imposing an aspect ratio on them. This is virtually equivalent to proceeding with a mechanical compression of an isotropic structure in a given direction. Note that this solution seems to be the closest to the physical reality as it is likely that the preferential orientation of the porous network that is observed on some microstructures is due to the high pressure imposed during the manufacture of ceramics.

We impose a preferential orientation to the IGB by applying an affine transformation to an isotropic tessellation. The following transformations are performed:

$$\boldsymbol{m} \rightarrow \hat{\boldsymbol{m}} \quad \text{with} \quad \hat{m_k} = \frac{1}{a_k} m_k \quad \text{and} \quad k = 1\,(x),\ 2\,(y),\ 3\,(z) \tag{2}$$

where $\boldsymbol{m}$ is the position vector of a point on the RVE and a_k is the renormalized aspect ratio (we impose $\prod_{l=1}^{3} a_l = 1$).

The criterion of the tessellation is thus modified. Indeed, in the case of a Voronoi tessellation, the distance formulation used in the criterion that allows to evaluate if a point $\hat{\boldsymbol{m}}$ belongs to the granule of center $\hat{\boldsymbol{c}}$ becomes:

$$\|\hat{\boldsymbol{m}} - \hat{\boldsymbol{c}}\|^2 = \sum_{l=1}^{3} \frac{(m_l - c_l)^2}{a_l^2} \tag{3}$$

3.2. Optimization of microstructure generation parameters

3.2.1. Optimization algorithm

In Section 3.1.1, the method developed to generate virtual microstructures with inter-granules porosity was presented. As explained above, the three degrees of freedom of this method are R_g, R_l and d_l. Moreover, if we consider an oriented microstructure, a degree of freedom corresponding to the aspect ratio ($AspR$) and directly linked to the renormalized aspect ratio (a_k) introduced previously is added. In practice, the coefficients $[a_1, a_2, a_3]$ are equal to $[(\mathrm{AspR})^{\frac{4}{3}}, (\mathrm{AspR})^{-\frac{2}{3}}, (\mathrm{AspR})^{-\frac{2}{3}}]$ which ensures $\prod_{l=1}^{3} a_l = 1$. These parameters constitute the arguments of the function we seek to minimize.

In Section 2.3, we have introduced the five different quantities that are used to characterize the microstructures, namely $H_{Intercepts}$, $H_{Intercepts,x}/H_{Intercepts,y}$, $H_{Matheron}$, H_{branch} and $H_{PrimaryBranch}$. They are used to evaluate the representativity of a virtual microstructure with respect to a given reference ceramic. For each quantity Q, the error returned (referred as ϵ_Q) is obtained by evaluating the difference between the cumulative distributions of the virtual microstructure and of the reference ceramic:

$$\epsilon_Q = \sqrt{\frac{\sum_{i=1}^{N_{class}} (H_{Q,i}^{ref} - H_{Q,i}^{virtual})^2}{N_{class}}} \tag{4}$$

where N_{class} is the number of classes for the calculation of the cumulative distribution (see Section 2.3.2), $H_{Q,i}^{ref}$ represents the ith value of the cumulative distribution of the reference microstructure and $H_{Q,i}^{virtual}$ the one of the virtual microstructure. The global error that is finally used is the average of the errors obtained with each of the five quantities.[6] We

[6] According to the implicit function theorem, we cannot expect to reach $\epsilon_g = 0$ since the number of input parameters is much smaller than the number of quantities we are trying to minimize.

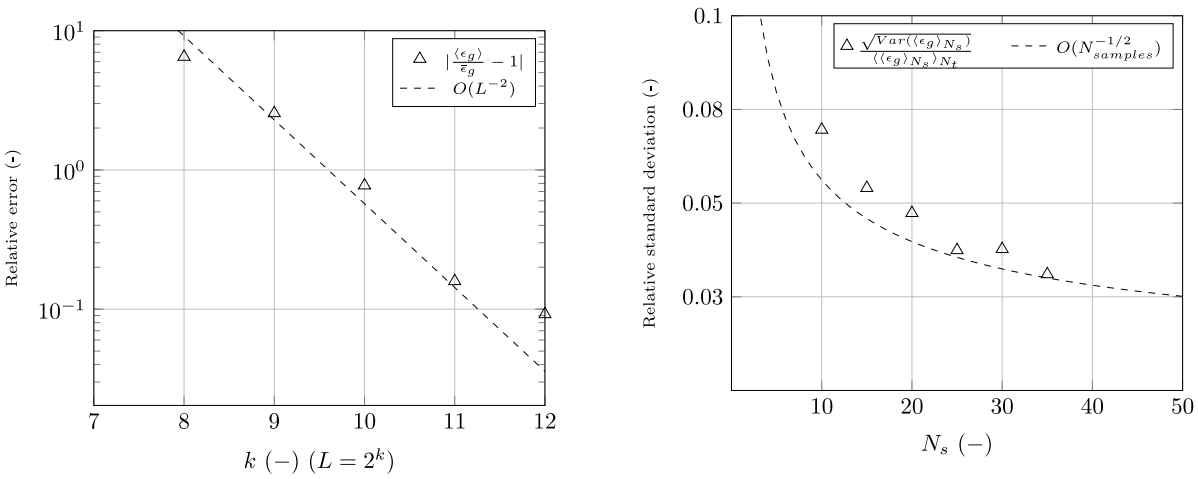

Fig. 7. Relative error on ϵ_g as a function of the RVE size (L) (on the left) and relative standard deviation on $\langle \epsilon_g \rangle_{N_s}$ as a function of the number of samples N_s for a RVE size $L = 2^{11}$ pixels and a number of tests $N_t = 50$ (on the right). The pixel size is 1.52 μm/pixel.

decided to give more weight to the error on the primary branches since the extension of the inter-granules pores has a first order impact on the thermal behavior of ceramics. We also gave more weight to the error on the branches because this parameter is very stable (many objects on the RVE and so little dependence on random effects) and it brings stability to the global error. Taking into account these considerations, the global error ϵ_g reads:

$$\epsilon_g = \frac{1}{7 + P^*}(\epsilon_{Intercepts} + \epsilon_{Matheron} + 2\,\epsilon_{Branch} + 3\,\epsilon_{PrimaryBranch} + P^*\,\epsilon_{RatioIntercepts}) \tag{5}$$

where $P^* = 0$ for isotropic ceramics (C_1, C_2, C_3) and $P^* = 1$ for the anisotropic ceramic (C_{3^*}). The choice of the exact values of the weights – here 1, 2 and 3 – remains of course arbitrary. The structure of the implemented optimization process is detailed in Appendix B. Since our optimization algorithm is performed on quantities extracted from geometrical objects that rely on random processes, we could have considered to employ minimization functions made especially for that. However, we preferred to use a more classical (deterministic) method and, to support this choice, we present in the next section a study of the variance of the error returned by our algorithm.

3.2.2. Study of the numerical and random errors

To ensure that the size of the RVE is sufficient so that the magnitudes measured on the tuned microstructures are typical of the whole mixture on average (Hill, 1963), we studied the evolution of the relative error on ϵ_g with respect to the infinite RVE solution (see (6)) as a function of the RVE size. This study was carried out for a given point (R_g, R_l and d_l are fixed) representative of what is encountered during the optimization process when we are looking to emulate the ceramic C_3. To get rid of the random effects (we focus on this aspect below) we average the results obtained over 50 generated microstructures. These independent microstructures are obtained by modifying the seed of the pseudo-random number generators used for the drawing of the cells and of the delimiting spheres. The relative error is given by the following equation:

$$Relative\ \ error = \left| \frac{\langle \epsilon_g \rangle}{\bar{\epsilon}_g} - 1 \right|, \tag{6}$$

where $\bar{\epsilon}_g$ is the solution obtained when $L \to \infty$. As the computational requirements quickly become important when L increases, we used for $\bar{\epsilon}_g$ the value obtained when $L = 2^{13}$ pixels. Results are presented in Fig. 7. The relative error seems to decrease in $O(L^{-2})$, a trend for which we do not have a sound theoretical justification. To minimize this error while maintaining a reasonable RVE size, we set $L = 2^{11}$ pixels for the rest of the study.

As previously mentioned (see Section 3.2.1), since the used microstructure generation algorithm is based on random processes, a rather large dispersion is expected on the measured quantities. One way to damper the random effects is to generate a certain number of samples (N_s), that are independent microstructures, for each point studied in order to extract averaged quantities. With a fixed RVE size of $L = 2^{11}$ pixels and a fixed number of tests $N_t = 50$, we studied the evolution of the relative standard deviation on the average of ϵ_g over N_s ($\frac{\sqrt{Var(\langle \epsilon_g \rangle_{N_s})}}{\langle \langle \epsilon_g \rangle_{N_s} \rangle_{N_t}}$) as a function of the number of samples (Fig. 7). As predicted by the Central Limit Theorem, the standard deviation decreases in $O(N_s^{-1/2})$. The observed deviation is quite important when the number of samples is low which leads to a high variability on the calculated error, hence the need to average over a large number of samples. We finally fixed N_s to 20 for the optimization process which provides a relative standard deviation lower than 5 %.

3.2.3. Tuned microstructures

We used the optimization process presented in Section 3.2.1 to find the best generation parameters. As an example, Fig. 8 illustrates the evolution of the error ϵ_g obtained by varying R_g after optimizing R_l and d_l for the ceramic C_3. A minimum appears quite clearly around $R_g = 30$ with a linear evolution before and after this minimum. Thus, the optimization process seems to have converged to the global minimum of our function.

Table 2 presents the optimized generation parameters obtained with the algorithm for each reference ceramic. We notice that the parameter that mainly varies for the generation of the different tuned microstructures is the density of delimiting spheres. The main differences between the microstructures are therefore due to the linear density of cracks. We also notice that the size of the delimiting spheres is stable, so there seems to be a characteristic size for the different studied ceramics which could be associated with an average spacing between the cracks. This average spacing could correspond to an effective size of the granules, a size of the granules obtained once the IGB network cracked. Let us specify that the parameter we introduced to define the radius of the granules (R_g, see Section 3.1.1) corresponds to a theoretical granule radius obtained when the IGB is fully cracked.

To illustrate the different obtained microstructures, an enlarged view on the cross-section of each tuned microstructure is drawn in Fig. 3. Also, a 3D view of the tuned microstructures is presented in Fig. 9.

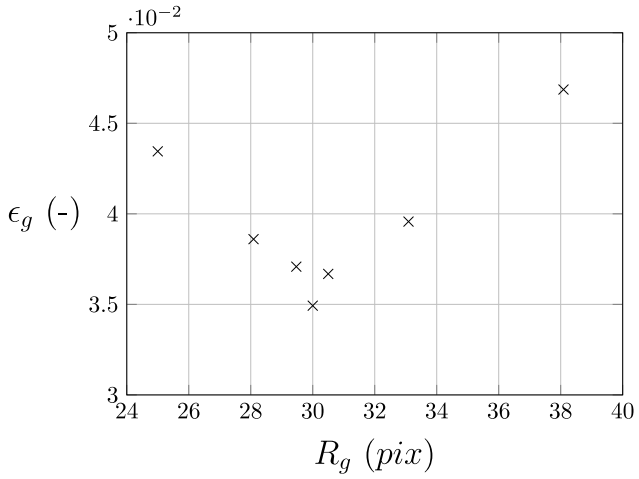

Fig. 8. Evolution of ϵ_g obtained by varying R_g (R_l and d_l are optimized). The pixel size is 1.52 µm/pixel.

Table 2
Parameters obtained with the optimization process for the generation of tuned microstructures associated with the reference ceramics.

	$C_{1,tuned}$	$C_{2,tuned}$	$C_{3,tuned}$	$C_{3^*,tuned}$
R_g (pix)	24.6	24.4	30	25
R_l (pix)	37.8	40.3	38.3	37.8
d_l (–)	2.2	1.89	1.1	1.06
$AspR$ (–)	/	/	/	1.46

The classification of the microstructures from weakly to strongly branched crack network is consistent with that observed on the reference ceramics. To study in more detail the evolution of the different quantities obtained by characterization on the tuned microstructures, the cumulative distributions that are used for the calculation of the different errors are plotted in Fig. 5. The consistency between the cumulative distributions of the tuned microstructures and those of the reference ceramics is remarkable. The most difficult parameter to optimize is that of Matheron's 2D granulometry. Indeed, the slopes of the Matheron size distributions of the tuned microstructures are systematically steeper than those of the cumulative distributions of the reference ceramics. It should be noted that this is in part due to the fact that we have prioritized the optimization of the quantities associated with the lengths of the branches and of the primary branches by controlling the weighting of the different parts of ϵ_g. This is also due to the particular scheme chosen for the generation of the IGB which leads to flat and regular inter-granules boundaries (see Section 3.1.1). That could certainly be improved by modifying the point process for the seeds of Voronoi grains, or by means of Laguerre polyhedra or even locally anisotropic tessellations (Gasnier et al., 2018b). We will see in Section 4 that the relatively simple choices adopted here yield excellent predictions of effective thermal properties. This is why we did not test these alternatives.

As a conclusion, the presented generation method coupled with the developed optimization algorithm allows to generate tuned microstructures which, based on the quantities retained for the characterization, reproduce well the microstructures of the reference ceramics. We propose in Section 4 an original approach to evaluate the representativity of the generated microstructures which is based on a comparison of their 2D thermal behavior with that of the reference ceramics cross-sections.

4. 2D thermal behavior computations to assess the realism of the virtual microstructures

In the work reported here, we seek to simulate the thermal response of 2D cross-sections extracted from 3D microstructures. This work presents a strong interest as the thermal answers obtained on 2D sections of tuned microstructures can directly be compared to those obtained on cuts of the reference ceramics ($C_1, \dots, C_{3^*}$).

4.1. Full-field simulations

To evaluate the 2D thermal behavior of the reference ceramics and of the tuned microstructures, full-field simulations are performed on the processed images obtained from their cross-sections (Figs. 3) using the FFT method. This method was originally proposed by Moulinec and Suquet (Moulinec and Suquet, 1998) and is highly interesting as it does not require meshing. However, this method presents difficulties to converge and especially when studying crack-like objects. The convergence can be ensured by using filters as presented in Willot et al. (2014) and, following Gasnier et al. (2018a), by giving a minimum thickness to the cracks (higher than $\sqrt{2}$ pixels in 2D, Meynard et al., 2022). Consequently, we have fixed the thickness of the cracks to five pixels in this study to avoid any convergence problem. Let us specify that the thickness of the cracks does not really affect the comparison of the thermal behavior since it is identical for the real microstructures (processed microstructures of the reference ceramics) and the tuned ones. To obtain a thickness of 5 pixels, a dilation step with diamond-like structuring elements of a 2-pixel size is performed on the skeletonized images, either real or tuned.

In this study, the cracks are considered insulating ($\lambda = 10^{-6}$ W m^{-1} K^{-1}) and the thermal conductivity of the solid matrix is fixed at 9.3 W m^{-1} K^{1} which is a value consistent with the thermal conductivity of UO_2 at 50 °C. The temperature gradient imposed in these FFT simulations is arbitrarily fixed since it does not affect the normalized quantities in linear thermics. Moreover, the Knudsen or radiative effects are not investigated since our objective is to give a first estimate of the thermal behavior of microstructures by maximizing the insulating role of porosity.

We are particularly interested in two quantities obtained with FFT simulations. The first one is the effective thermal conductivity denoted by $\tilde{\lambda}$ and which is obtained from the heat flux density ($\mathbf{q}$) and temperature gradient ($\boldsymbol{\nabla}$T) fields:

$$\tilde{\lambda} = -\frac{\langle \mathbf{q} \rangle_{\mathrm{RVE}}}{\langle \boldsymbol{\nabla} \mathrm{T} \rangle_{\mathrm{RVE}}} \tag{7}$$

Where the operator $\langle . \rangle_{\mathrm{RVE}}$ represents the spatial average over the RVE. The second studied quantity is the normalized flux which corresponds to the flux divided by its spatial average over the RVE in a given direction (here the direction x):

$$\boldsymbol{\Phi}_{norm,x} = \frac{\boldsymbol{\Phi}_x}{\langle \boldsymbol{\Phi}_x \rangle_{\mathrm{RVE}}} \tag{8}$$

The FFT simulations are performed on real and tuned microstructures (processed images with dilated skeletons as mentioned above) and periodic conditions are imposed at the edges of the RVE. These boundary conditions are consistent for tuned microstructures which are by nature periodic (see Section 3), but not for real microstructures which are not. To overcome this problem, an oversampling method is used (Gloria, 2011). What is done is that, for real microstructures, the simulations are performed on the whole window but the homogenized quantities are calculated on a subwindow. That allows to damper the boundary effects by neglecting the values of quantities of interest near the edges of the images. The way we resize the images is illustrated Fig. 10.

To evaluate the effect of this oversampling method, we calculated the 2D effective thermal conductivity of the ceramic C_{3^*} obtained by imposing a temperature gradient along x when varying the rescale size used. Equivalent results were obtained when imposing a temperature gradient along y. The effect of oversampling (along x and y) on the simulated effective conductivity is reported in Table 3.

The effects of oversampling are quite important on this microstructure as an overestimation of the thermal conductivity of about 8 % is

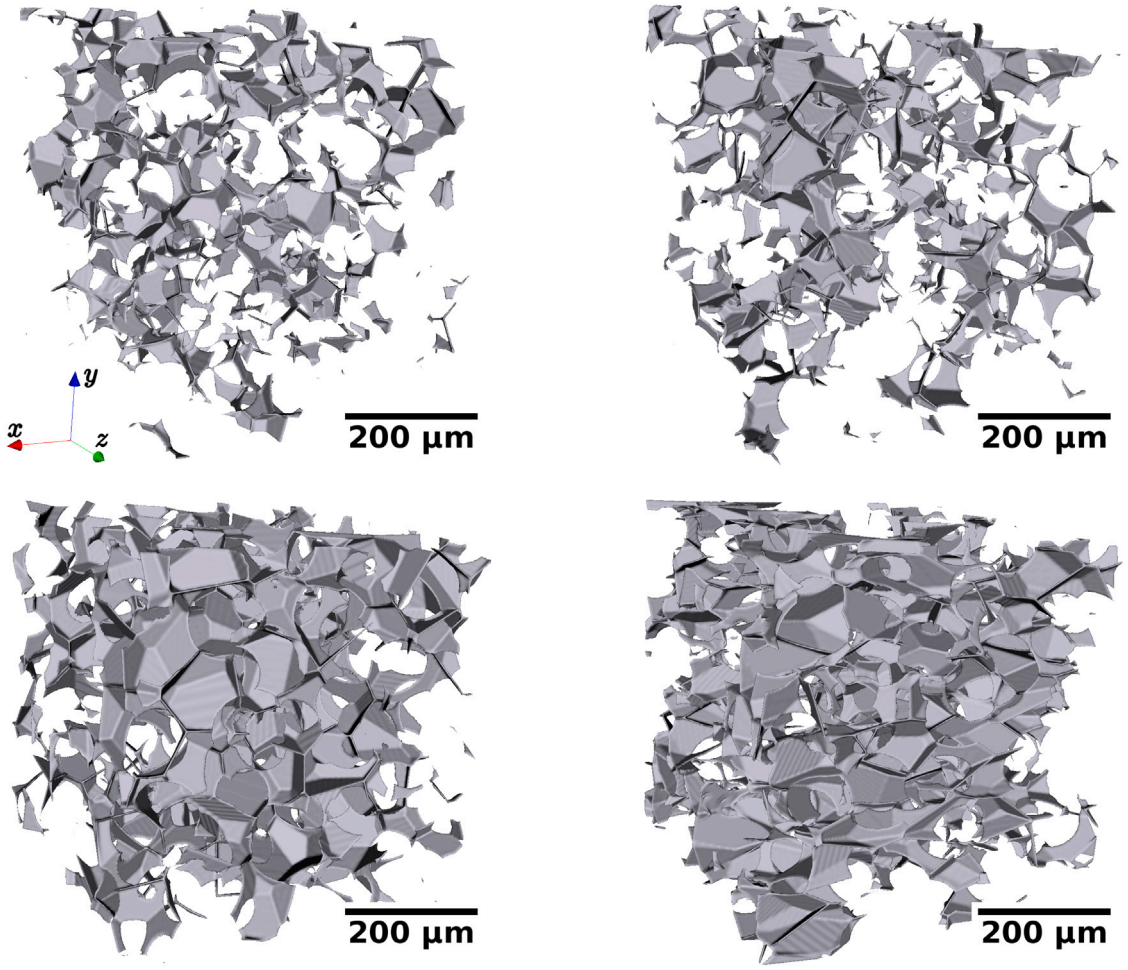

Fig. 9. 3D enlarged views (400x400x400 pix^3) on the tuned virtual microstructures associated with the ceramics C_1, C_2, C_3 and C_3^* respectively.

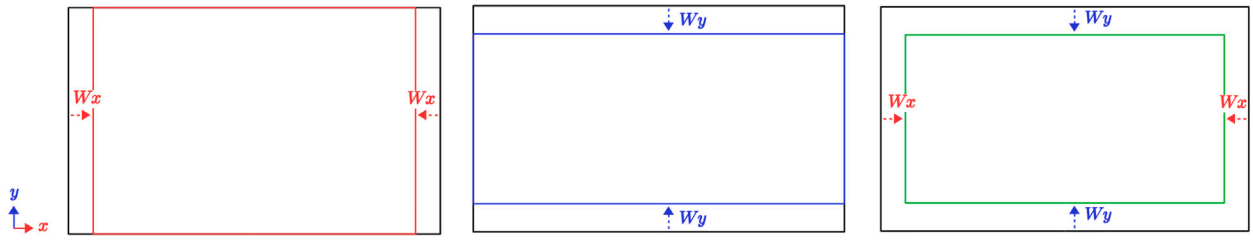

Fig. 10. Diagram illustrating the resizing of the window when applying the oversampling method according to x (on the left), to y (on the center) and to x and y (on the right).

Table 3
Effect of windowing on the effective conductivity (W m^{-1} K^{-1}) obtained by imposing a temperature gradient along x ($\tilde{\lambda}_x$) and evaluated by simulation on C_{3^*}. The pixel size is 1.52 µm/pixel.

H (pix)	0	50	100	200	250
$\tilde{\lambda}_x$ $(W_x = H, W_y = 0)$	5.85	5.82	5.82	5.82	5.81
$\tilde{\lambda}_x$ $(W_x = 0, W_y = H)$	5.85	5.64	5.48	5.45	5.47
$\tilde{\lambda}_x$ $(W_x = W_y = H)$	5.85	5.59	5.45	5.40	5.39

observed. These effects are much more marked when the windowing is applied according to y than according to x which is consistent since the processed images of the reference microstructures are much larger along x than along y (see Section 2.2). It should also be noted that these effects are particularly important for ceramics with a highly extended porous network and that they are negligible for those with a poorly extended porous network. Indeed, an equivalent study carried out on C_1 revealed a variation of the effective conductivity of about only 1 %. Since windowing is necessary for highly porous ceramics (significant variation in effective conductivity up to $W = 200$ pixel, see Table 3), in the following, the scale value for the windowing is set to 200 pixels along x and y ($W_x = W_y = 200$).

Now that we have presented the method as well as the conditions used for the simulations, we discuss in the next section the thermal behavior of the reference ceramics and in particular their thermal conductivity.

4.2. Thermal behavior of 2D microstructures

It can be noted that, for the study of the thermal behavior of ceramics C_1, C_2 and C_3, the temperature gradient is imposed along the y direction but this is not really important since the crack network of these ceramics does not present a strong preferential orientation.

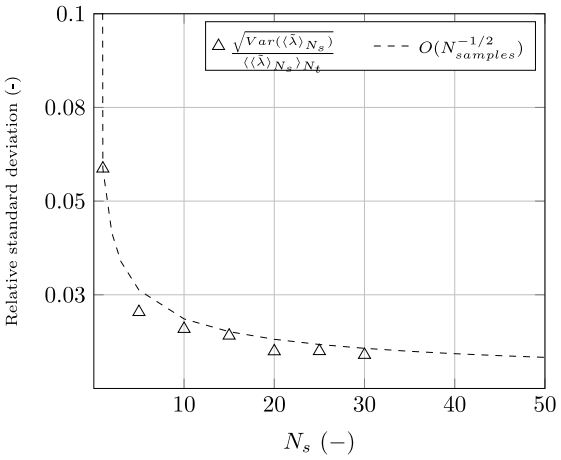

Fig. 11. Relative standard deviation on $\tilde{\lambda}$ as a function of the number of samples N_s obtained for a RVE size of $L = 2^{11}$ pixels and a number of tests $N_t = 50$ (the pixel size is 1.52 µm/pixel).

Indeed, for these ceramics, the ratio between the effective conductivity obtained when the temperature gradient is imposed along the x direction and along the y direction ($\tilde{\lambda}_x/\tilde{\lambda}_y$) equals to one within 3 %.

However, for the ceramic C_{3*} which presents a preferential orientation, the direction according to which the gradient is imposed is crucial. We then study the thermal behavior of this ceramic by imposing a temperature gradient both along x and along y.

4.2.1. Effective thermal conductivity

Before proceeding to the study of the thermal behavior, we verified that the relative standard deviation associated with the effective conductivity was at least comparable to those previously evaluated on Sections 2.3.3 and 3.2.2. The size of the RVE is fixed to $L = 2^{11}$ pixels as discussed in Section 3.2.2. For $N_s = 30$, the relative standard deviation on the effective conductivity is about 1 % (Fig. 11). The behavior of the effective conductivity is then much more stable than that of the previously studied quantities.

The simulated 2D effective thermal conductivities of the real and tuned microstructures are reported in Table 4. As expected, the porous network plays an important role in the degradation of the thermal conductivity of ceramics so that the simulated conductivities decrease when the open porosity increases (as a reminder, see Table 1 to find the open porosity of reference ceramics). In addition, the effective conductivities calculated on the tuned microstructures are in good agreement with those calculated on the real microstructures. Indeed, the maximum deviation is lower than 2 % (except for the effective thermal conductivity along y for C_{3*} where it is about 4 %). It is interesting to note that ceramics C_3 and C_{3*} have very different effective conductivities in spite of a similar concentration of cracks. This demonstrates the importance of considering the orientation of the cracks in the thermal simulations. For the ceramic C_{3*} which presents a preferential orientation along x, the ratio between the effective conductivity along x and that along y simulated on the real microstructure is $\tilde{\lambda}_x/\tilde{\lambda}_y = 1.37$. This represents a significant difference in the thermal behavior along these two directions and that is consistent with the anisotropy measured on this ceramic thanks to the ratio of the intercepts (Fig. 5). The tuned microstructure reproduces well this behavior, even if the effect of the orientation of the crack network is slightly less important ($\tilde{\lambda}_x/\tilde{\lambda}_y = 1.3$ for this tuned microstructure).

4.2.2. Heat flux map and histograms

To get further in the comparison of the 2D thermal behavior of the reference ceramics to that of the tuned ones, we now compare the simulated heat flux fields. These fields are reported in Fig. 12. As explained above, the temperature gradient is prescribed along the y direction (ϕ_{norm} denotes $\phi_{norm,y}$) but similar heat flux map are obtained when the temperature gradient is prescribed along the x direction.

Table 4
2D effective thermal conductivity (W m^{-1} K^{-1}) of the real and tuned microstructures. The pixel size is 1.52 µm/pixel.

	C_1	C_2	C_3	C_{3*}	
	$\tilde{\lambda}_y$	$\tilde{\lambda}_y$	$\tilde{\lambda}_y$	$\tilde{\lambda}_y$	$\tilde{\lambda}_x$
Real	8.12	7.30	5.27	3.94	5.40
Tuned	8.15	7.43	5.28	4.10	5.32

Fig. 12 shows good agreement between the real and tuned heat flux fields. For a more quantitative approach, heat flux distribution histograms are studied (Fig. 13). The differences between the normalized heat flux distribution histograms of the reference ceramics are an interesting testimony of the differences between their crack networks. The more extended the crack network is, the flatter the histogram will be. That is because the heat flux distribution is less homogeneous. Conversely, when the crack network is not very extended, some heat flux values are over-represented because there is little variation in the flux and the histogram will present a peak as it clearly appears on the histogram of ceramic C_1. We can notice that the tuned microstructures reproduce in a suitable way the thermal behavior of the reference microstructures.

Quite similar results are obtained in the case of an oriented microstructure (C_{3*}). It is interesting to note that the heat flux distribution histogram obtained when the gradient is imposed along x (in the direction perpendicular to the orientation of the cracks) is significantly flatter than the one obtained when the gradient is imposed along y (Fig. 14). The effect of the orientation of the crack network on the thermal behavior of the ceramics is thus well marked. The tuned microstructure reproduces well the thermal behavior of the C_{3*} ceramic and its anisotropic character.

The study of the 2D thermal behavior of reference ceramics also allows to highlight the non-homogeneous spatial distribution of cracks. Indeed, crack clusters may explain the presence of large blue areas in which the normalized flux is nearly zero. This is particularly marked for the microstructures with a highly extended crack network (C_3 on Fig. 12 and C_{3*} on Fig. 14). These zones are called "dead zones" in the rest of the study since they constitute important barriers for the heat flux. These dead zones can be seen on the histograms of the normalized flux distribution by the presence of a peak for zero flux values (Figs. 13 and 14). The effect of the presence of clusters of cracks on the homogeneous thermal properties of the microstructures is not obvious because on the one hand the presence of regions in which the heat flux does not circulate can degrade the thermal conductivity but at the same time, the fact of concentrating the cracks in certain regions allows the appearance of paths privileged by the heat flux.

In the next section we study more precisely the dead zones by looking at their spatial distribution.

4.2.3. Study of "dead zones" using the covariogram

The covariance is a tool that allows to characterize objects and particularly to study their shape, their spatial distribution or their orientation (Jeulin, 2000; Torquato and Haslach, 2002; Kanit et al., 2003; Drach et al., 2016). In practice, the covariance is a comparison between an image and its translate according to a vector $\boldsymbol{h}$. More precisely, the covariance $C_{ij}(\boldsymbol{h})$ or phase i/phase j gives the probability that two points $\boldsymbol{m}$ and $\boldsymbol{m} + \boldsymbol{h}$ belong respectively to phase i and j. The covariance is independent of the choice of $\boldsymbol{m}$ (stationarity) but it depends strongly on the vector $\boldsymbol{h}$, defined by a distance h and an angle θ. The covariance has two remarkable properties:

- By construction, $C_{i,i}(0)$ is equal to the volume fraction of the phase i.

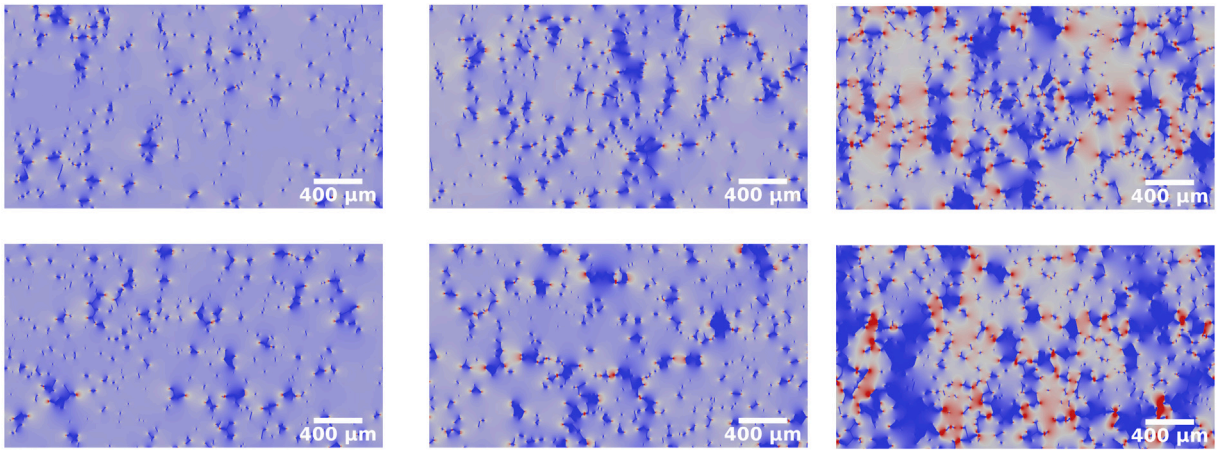

Fig. 12. Heat flux fields obtained on the real (top) and on the tuned (bottom) microstructures (From left to right: C_1, C_2 and C_3). The temperature gradient is prescribed along the vertical direction. The color scale goes from blue when $\phi_{norm} = 0$ to red when $\phi_{norm} = 3$.

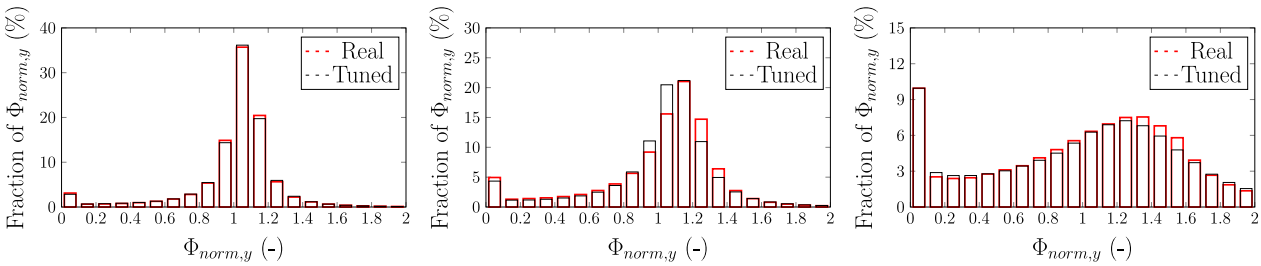

Fig. 13. Heat flux histograms obtained on the real and tuned microstructures (C_1, C_2 and C_3).

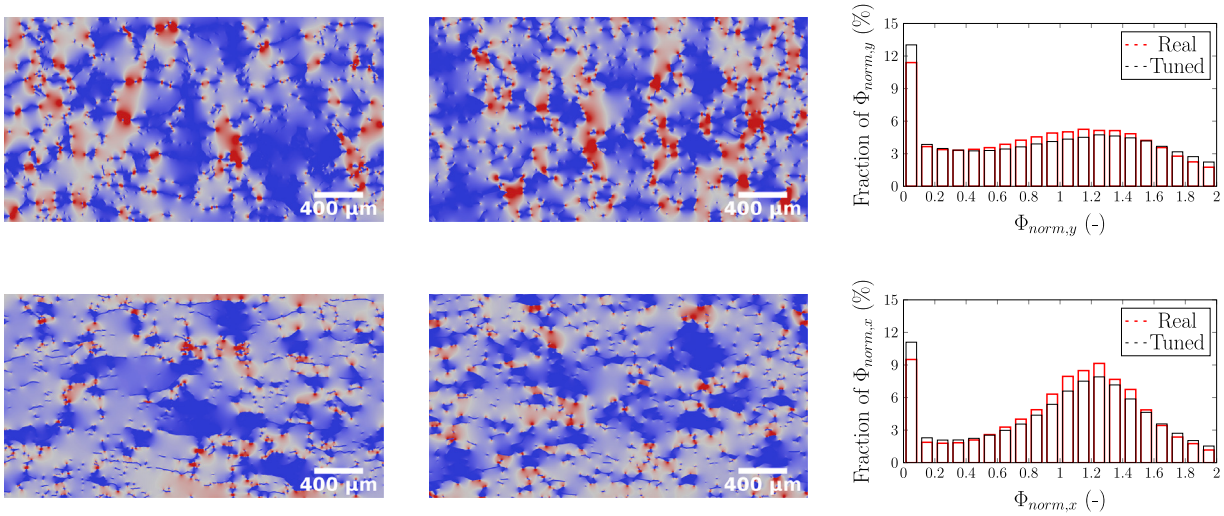

Fig. 14. Heat flux map and histograms obtained by imposing a temperature gradient along x (bottom) and along y (top) on the real (left images) and tuned (right images) microstructures associated with the reference ceramic C_{3^*}.

- If the domain for the study is sufficiently large and if there are not long-range correlations (which is our underlying assumption), then $C_{i,j}(h,\theta) \to C_{i,i}(0,\theta)\,C_{j,j}(0,\theta)$ when $h \to \infty$.

In our case, the covariance is applied to two-phase images obtained after binarizing the heat flux maps by applying a threshold on the cumulative heat flux histograms. The threshold value to be applied was chosen by studying the effect of thresholding on the shape of the dead zones obtained after binarization. The objective was to find the areas identified on the heat flux maps and to keep their localized character. Using this method, the threshold value was arbitrarily set at $\phi_S = 0.65$. The binarized images obtained for the different real and tuned microstructures are presented Fig. 15.

As expected, the density of the pore network of ceramics has a remarkable influence on the properties of the dead zones since they become wider when the linear density of cracks increases. The fact that we imposed a temperature gradient along y when simulating the thermal behavior of these microstructures is clearly visible. Indeed, the dead zones are more extended in this direction. The binarized images show good agreement between real and tuned microstructures even if the tuned microstructure associated with ceramic C_3 seems to feature larger dead zones than the real one.

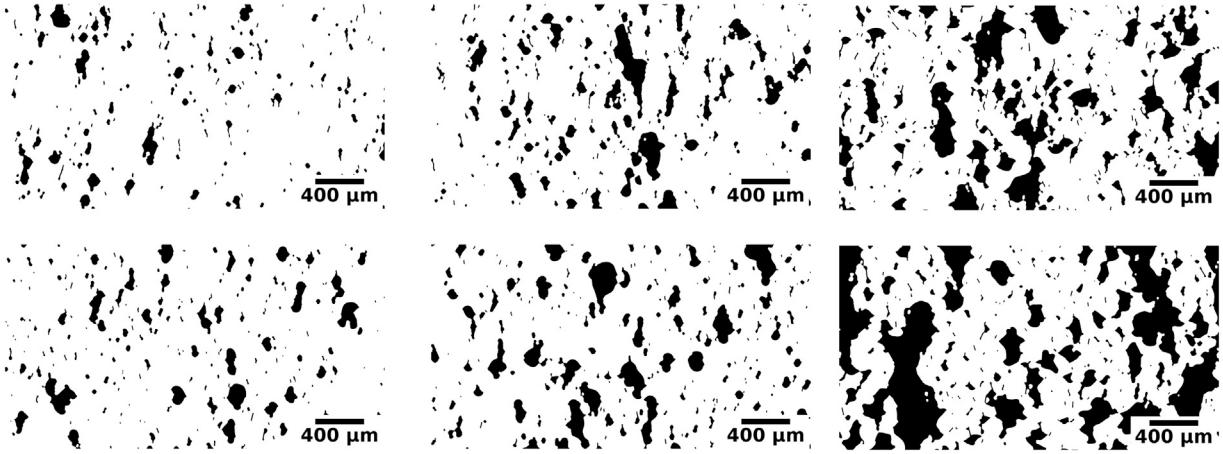

Fig. 15. Binarized heat flux map images obtained on the real (top) and on the tuned (bottom) microstructures (From left to right: C_1, C_2 and C_3).

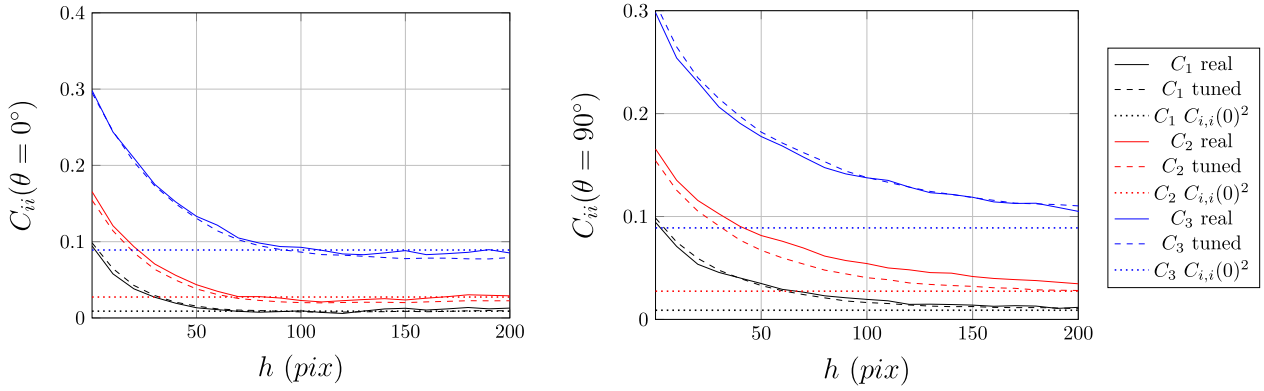

Fig. 16. Covariances in the x ($\theta = 0°$, on the left) and y ($\theta = 90°$, on the right) directions applied on the binarized heat flux images of the real and tuned microstructures. The pixel size is 1.52 µm/pixel.

The covariances along x ($\theta = 0°$) and along y ($\theta = 90°$) obtained on the binarized heat flux images are plotted Fig. 16. Let us specify that, in order to highlight the area in which the covariance varies, the figures presenting the covariances are limited to $h = 200$ pix. We can notice that we find back, by observing the values at the origin ($C_{i,i}(0)$), that the evolution of the surface fraction of the dead zones is correlated with the increase in the density of the porous network of the ceramics. This surface fraction increases from 10% (C_1) to nearly 30% (C_3). We can also underline, by looking at the slope of the covariances when h is large enough ($C_{i,i}(h, \theta)$ when $h \to \infty$), that they converge well towards $C_{i,i}(0, \theta)^2$. This means that the size of the RVE is sufficient to study the dead zones.

The covariances calculated on the tuned microstructures are very close to those estimated on the reference ceramics. Let us recall that the images presented here are, for reference ceramics, enlarged views of significantly larger images (see Section 2.2) and, for tuned microstructures, sections taken from a large number of generated microstructures (see Section 3.2.2). This justifies that, despite the differences that can be observed between the binarized images of the real and tuned microstructures, the averaged quantities (here the covariance) can be close.

The same study was conducted for the C_{3*} ceramic in order to evaluate the effect of the crack network orientation on the dead zone characteristics. The corresponding results are reported in Appendix C. We find the same behavior as was identified on non-oriented ceramics, i.e. that the densification of the pore network leads to an increase in the size of the dead zones.

5. Conclusions

A methodology has been presented to optimize the generation of 3D virtual microstructures in order to mimic the inter-granules porosity of reference ceramics observed on 2D images. These ceramics have a more or less extended and branched porous network which can be assimilated to a network of cracks distributed at the joints between the granules.

A thorough characterization of the porous network of the reference ceramics was carried out. An image processing protocol was set up to convert optical microscopy images into skeletonized binary images from which it is possible to extract information about the porous network. Five criteria were retained to describe this network: the length of the intercepts which makes it possible to evaluate the concentration in cracks, the ratio between the intercepts calculated in the crack orientation direction (if the crack network of the considered ceramic has a preferential orientation) and those calculated in the perpendicular direction which is useful to characterize the anisotropy, the radius of Matheron's 2D granulometry by circles which allows to approach the spatial distribution of the cracks, the length of the branches and the length of the primary branches which are used to give information on the dimensions of the cracks, regarding both the individual components at grain interfaces and their branching with their neighbors.

The general principles of the method for generating 3D virtual microstructures with crack-like pores distributed along the inter-granules boundaries, proposed by Meynard et al. (2022), has been recalled. This method allows to generate a large variety of microstructures by playing with only three input parameters. An optimization procedure

has been developed to determine the generation parameters that allow to obtain tuned microstructures as faithful as possible to the reference ceramics. This procedure is based on a comparison of cross-sectional images of the porous network of the generated microstructures with that of the reference ceramics using the identified descriptor parameters. This procedure provided good results as the generated tuned microstructures have properties close to those of the reference ceramics (Fig. 5), except for the Matheron's granulometry. The systematic character of the developed optimization process has made it possible to study different ceramics of interest without much effort. The results of this optimization process are 3D morphological models of the porous networks more or less extended into these different ceramics as illustrated by the 3D rendering in Fig. 9. Furthermore, it will be possible to use this procedure in the future to study a wider set of materials, exhibiting a continuous range of microstructural features between the here considered extreme cases, in particular in the context of the study of evolving materials.

To further validate this optimization process before using it to simulate the thermal conductivity of these 3D microstructures, 2D full-field numerical simulations (based on the FFT method) have been performed on processed images of reference ceramics and on cross-sections extracted from the tuned 3D microstructures. These 2D simulations are used as a further validation of the tuned model, involving not only the partial set of 2D geometrical features used to fit the model, but also the whole features involved in the thermal properties of a 2D heterogeneous medium. Of course, it is not sufficient to validate the performances of the model regarding full 3D thermal properties, but provides an additional, not conventional, way to confirm the similarity of the virtual 2D cross-section with the real ones. This validation is performed on effective 2D properties, but also and more importantly, on local field statistics both in terms of distribution function and spatial correlations. With that respect, it is worth to remark that these 2D computations are related to 3D microstructures with ribbon cracks infinite in the direction perpendicular to the studied plane. Thus, the effect of cracks on the thermal conductivity is here exacerbated since ribbon cracks fully stop the thermal flux. The good agreement is thus satisfactory in this rather challenging situation and provides some confidence on the pertinence of the 3D simulations planned for the future, even though, of course, it is not a proof of their efficiency.

Indeed, work is in progress to further validate the developed model by comparing 3D simulations with experimental results. In this way, new considerations must be made for the model, notably to take into account the porous network at different scales (the one studied so far enriched by a porosity at small scale which is associated with the interfering objects and thus eliminated during the image processing described in Section 2.2). In addition, thermal diffusivity measurements are currently performed on real ceramics at different temperatures and in different gas environments. The developed numerical model will finally allow to understand the thermal behavior of ceramics in temperature ranges which are currently out of reach of the experiment.

We study here conductive properties as we are interested in the thermal behavior of the microstructures but it could be interesting to continue the comparison between 2D sections of virtual microstructures and processed images of the reference ceramics to study other effective properties such as permeability or elasticity. In these future studies, more complex pores geometrical supports may be tested by using a different grain generation process such as, for example, the Johnson and Mehl (1939) tessellation, which leads to grains that are not necessarily convex neither of polyhedral shape.

Declaration of competing interest

The authors declare that they have no known competing financial interests or personal relationships that could have appeared to influence the work reported in this paper.

Data availability

Data will be made available on request

Acknowledgments

The authors are grateful for the financial support provided by the French Alternative Energies and Atomic Energy Commission (CEA). They are also grateful to Ph. Sornay (CEA) who manufactured the different ceramics studied in this work. Numerical characterizations were realized with the open-access image analysis software Fiji (Schindelin et al., 2012) version 2.1.0/1.53c launched with Java 1.8.0. The microstructures and the FFT computations were produced with version 1.0 of the MEROPE software and with version 1.8 of the TMFFT software (components of the PLEIADES platform), respectively.

Appendix A. Assessment of the lengths of branches and primary branches

The principle for the calculation of lengths with *Crackcut* is to discretize the objects into segments as long as possible but with a length smaller than l_{max}. In practice they have all almost a length l_{max} (it is not exactly l_{max} because of pixelization), except the last segment which is shorter to fit the actual end of the branche. Fig. A.17 shows how the *Crackcut* plugin works when applied to an isolated object (the principle is the same when several objects are present on the image). For reasons of readability of the image, the length l_{max} was chosen to be large enough for the segmentation to be visible. This explains why the segmentation is coarse in the chosen example while processing the illustrative primary branche.

The accuracy of this method relies on the choice of l_{max}. It must be small compared to the size of the objects considered (more precisely their radius of curvature) but large enough with respect to pixel size in order to get rid of the bias introduced by pixelization. To set the value of l_{max} to use in our study, we evaluated its influence on the cumulative distribution of the length of the branches and primary branches. As we can see in Fig. A.18, which provides an example for ceramic C_3, quite important discrepancies between the cumulative distributions are observed when $l_{max} = 1$ pixel and $l_{max} > 50$ pixels. This reveals a shortening of the objects when l_{max} is not small enough because of the elimination of geometric details (undulations) with a size below l_{max}. For values of l_{max} between 5 and 20 pixels, the cumulative distributions are very close and a quick analysis of the obtained images shows that they still remained very close to the original skeletons. Similar results were observed on the other studied ceramics. Thus, l_{max} is set at 10 pixels (15.2 µm). It is noticed that this size is equal to the diameter of the disks used to perform the morphological closing of the segmented cracks. Indeed the proposed image processing and object quantification routines are associated with this typical size of 15 µm. Details below this length are smoothed out but larger ones are kept so as to preserve the complexity of the pores geometry at grain scale. In addition, this size is sufficiently large with respect to pixel size, so that pixelization does not induce any significant bias.

Appendix B. Optimization algorithm structure

For isotropic ceramics (C_1, C_2 and C_3), we seek to minimize a function that takes three arguments as input (R_g, R_l and d_l) and returns as output an error (ϵ_g) that allows us to judge the quality of a virtual microstructure to reproduce certain parameters observed on a reference microstructure. To implement this optimization process, the optimize package of the scipy library (Virtanen et al., 2008) which provides several functions for minimizing objective functions has been used. The optimization is done under constraint as the input parameters

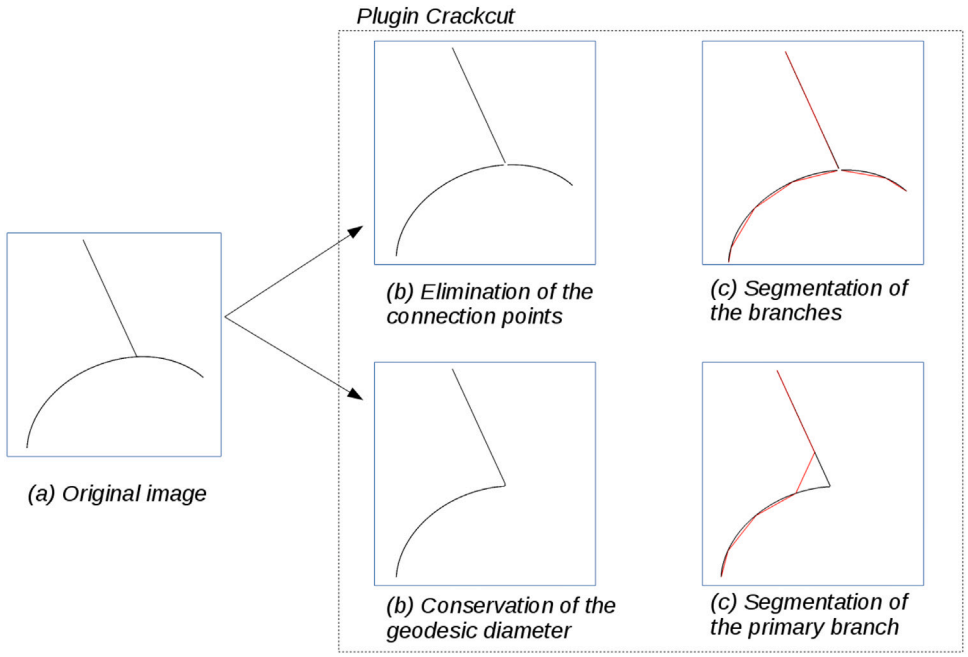

Fig. A.17. Diagram explaining how the *Crackcut* plugin works. The red segments show the discretization of the skeletons. Here l_{max} is deliberately chosen to be large enough for the differences between the original image and the segmented one to be visible.

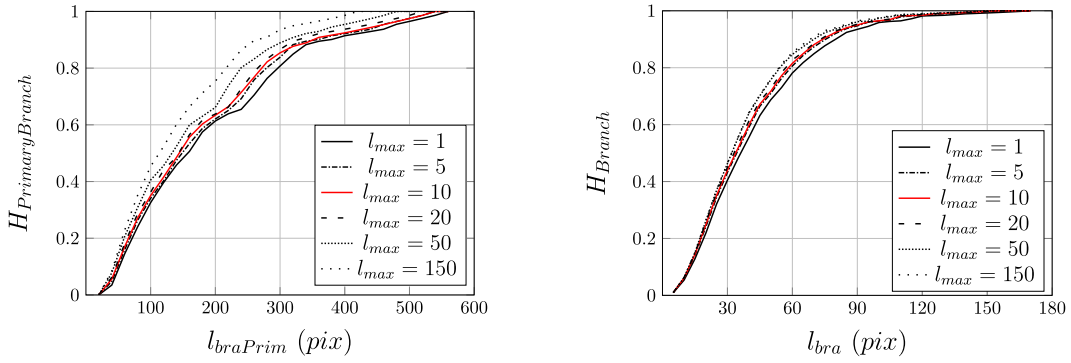

Fig. A.18. Influence of l_{max} on the cumulative distributions of length of the primary branches and branches measured with *Crackcut* on C_3. The pixel size is 1.52 μm/pixel.

are necessarily positive. The equation describing the structure of the optimization algorithm is the following:

$$\min_{R_g}\left[\min_{R_L}\left[\epsilon_g(R_g, R_L, d_l) + \min_{d_l}\left[\epsilon_{Intercepts}(R_g, R_l, d_l)\right]\right]\right], \tag{B.1}$$

$\epsilon_{Intercepts}$ and ϵ_g being defined by relations (4) and (5) respectively ($P^* = 0$ for ceramics C_1, C_2 and C_3). Three optimization loops are nested which allows for a sequential optimization and consequently the optimization of functions with only one input argument. For each loop, the Powell (1964) method implemented in the scipy.optimize.minimize library is used. Two strong choices were made in the structure of the algorithm. The first choice is to perform a sequential optimization on the three degrees of freedom. This leads to a loss of performance since a more direct path could be found but this choice was made to simplify the solving process since no solution could be found when the three input parameters were left free simultaneously. As we found that the length of the intercepts is very little dependent on the other input parameters (R_g and R_l), the second choice that was made is to optimize the innermost loop (d_l) only on the error on the intercepts.

For the anisotropic ceramic (C_{3*}), we seek to minimize a function that takes four arguments as input (R_g, R_l, d_l and $AspR$) and returns as output an error (ϵ_g) that takes into account the error on the ratio of the intercepts ($P^* = 1$ in relation (5)). As the ratio of the intercepts is also very little dependent on the other parameters (R_g and R_l), this quantity is minimized with respect to the additional aspect ratio parameter only. Then, the equation describing the structure of the algorithm becomes:

$$\min_{R_g}\left[\min_{R_L}\left[\epsilon_g(R_g, R_L, d_l, AspR) + \min_{d_l}\left[\epsilon_{Intercepts}(R_g, R_l, d_l, AspR)\right] + \min_{AspR}\left[\epsilon_{RatioIntercepts}(R_g, R_l, d_l, AspR)\right]\right]\right] \tag{B.2}$$

Appendix C. Ceramic C_{3*}: study of the "dead zone" (covariance)

The binarized images obtained from the heat flux maps simulated on the real and tuned microstructures as well as the covariances measured on these binarized images are shown Figs. C.19 and C.20.

As for non-oriented ceramics, the densification of the pore network leads to an increase in the size of the dead zones. We note that the effect of the orientation of the crack network is clearly visible since the dead zones are significantly wider when the temperature gradient is imposed along y (direction perpendicular to the preferential orientation of the cracks). This confirms that, when the heat flux is perpendicular to the

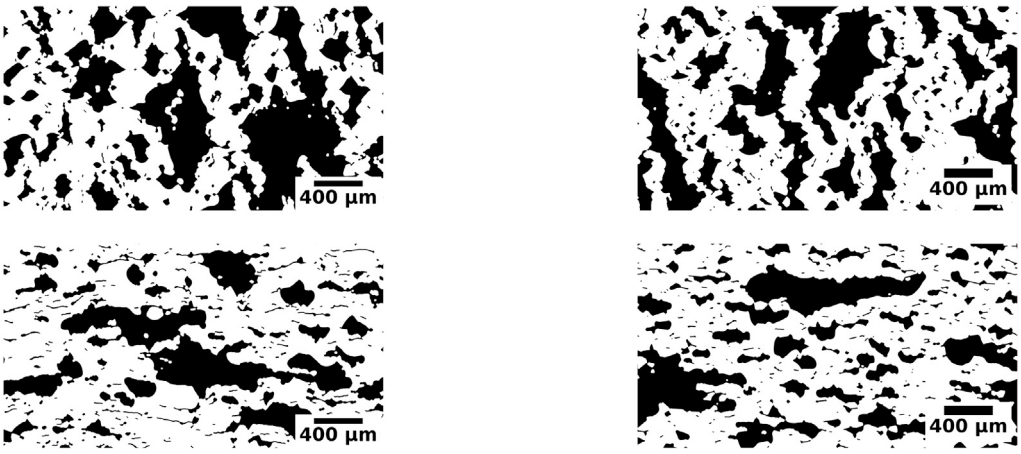

Fig. C.19. Binarized heat flux maps images obtained by imposing a temperature gradient along x (bottom) and along y (top) on the real (left images) and tuned (right images) microstructures associated with the reference ceramic C_{3^*}.

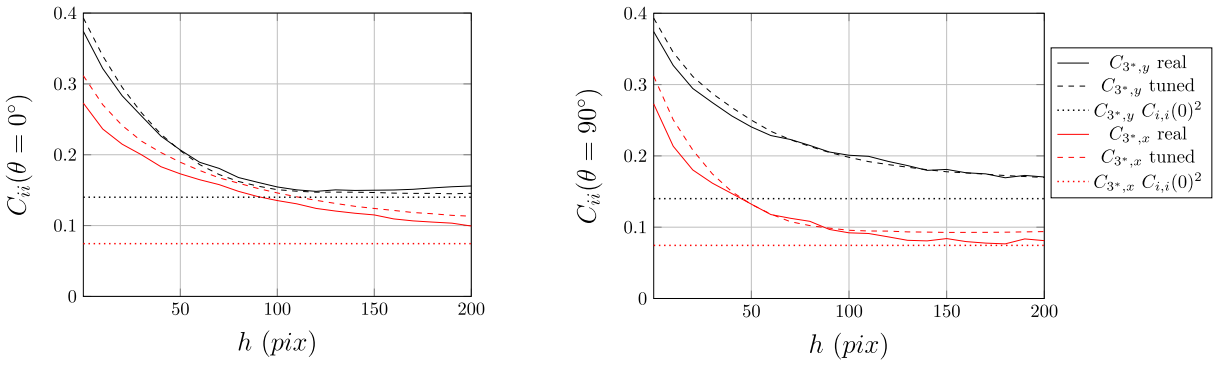

Fig. C.20. Covariances in the x ($\theta = 0°$, on the left) and y ($\theta = 90°$, on the right) directions obtained on the binarized heat flux images of the ceramics C_{3^*} with a temperature gradient imposed along x (in red) and along y (in black). The pixel size is 1.52 µm/pixel.

crack orientation, they constitute much more important barriers for the flux. It is interesting to underline that, by looking at the covariances, one could assume that the behaviors obtained by imposing a thermal gradient along x and along y are those of two different microstructures with significantly different pore network densities.

References

Abrams, H., 1971. Grain size measurement by the intercept method. Metallography (ISSN: 0026-0800) 4 (1), 59–78. http://dx.doi.org/10.1016/0026-0800(71)90005-X, URL https://www.sciencedirect.com/science/article/pii/002608007190005X.

Altendorf, H., Jeulin, D., Willot, F., 2014. Influence of the fiber geometry on the macroscopic elastic and thermal properties. Int. J. Solids Struct. (ISSN: 0020-7683) 51 (23), 3807–3822. http://dx.doi.org/10.1016/j.ijsolstr.2014.05.013, URL https://www.sciencedirect.com/science/article/pii/S0020768314001991.

Bailly, H., Menessier, D., Prunier, C., 1996. Le Combustible Nucléaire Des Réacteurs à Eau Sous Pression Et Des Réacteurs à Neutrons Rapides. CEA, Eyrolles.

Bargmann, S., Klusemann, B., Markmann, J., Schnabel, J.E., Schneider, K., Soyarslan, C., Wilmers, J., 2018. Generation of 3D representative volume elements for heterogeneous materials: A review. Prog. Mater. Sci. (ISSN: 0079-6425) 96, 322–384. http://dx.doi.org/10.1016/j.pmatsci.2018.02.003, URL https://www.sciencedirect.com/science/article/pii/S0079642518300161.

Bluthé, J., Bary, B., Lemarchand, E., 2021. Contribution of FE and FFT-based methods to the determination of the effective elastic and conduction properties of composite media with flat inclusions and infinite contrast. Int. J. Solids Struct. (ISSN: 0020-7683) 216, 108–122. http://dx.doi.org/10.1016/j.ijsolstr.2021.01.007, URL https://www.sciencedirect.com/science/article/pii/S0020768321000135.

Bruchon, J-F., Pereira, J-M., Vandamme, M., Lenoir, N., Delage, P., Bornert, M., 2013. X-ray microtomography characterisation of the changes in statistical homogeneity of an unsaturated sand during imbibition. Géotech. Lett. 3, 84–88. http://dx.doi.org/10.1680/geolett.13.00013.

Burger, W., Burge, M.J., 2008. Digital Image Processing: An Algorithmic Introduction using Java, first ed. In: Texts in Computer Science, Springer.

Coster, M., Chermant, J.L., 1989. Précis D'analyse D'images, twenty second ed. Presses Du CNRS, CNRS Plus. Paris.

Delafosse, J., Lestiboudois, G., 1976. Choix effectué par le CEA pour la fabrication des oxydes d'uranium et ses conséquences sur les performances du combustible. Colloque International sur la Fabrication Des éléments Combustibles Pour Réacteurs à Eau Et Plus Spécialement Son Incidence sur la Performance.

Dowek, R., Cagna, C., Noirot, J., Zacharie-Aubrun, I., Blay, T., Hanifi, K., Bienvenu, P., Roure, I., Cabié, M., Dumont, M., 2021. Determination of the pressure in micrometric bubbles in irradiated nuclear fuels. J. Nucl. Mater. (ISSN: 0022-3115) 543, 152591. http://dx.doi.org/10.1016/j.jnucmat.2020.152591, URL https://www.sciencedirect.com/science/article/pii/S0022311520311995.

Drach, B., Tsukrov, I., Trofimov, A., 2016. Comparison of full field and single pore approaches to homogenization of linearly elastic materials with pores of regular and irregular shapes. Int. J. Solids Struct. (ISSN: 0020-7683) 96, 48–63. http://dx.doi.org/10.1016/j.ijsolstr.2016.06.023, URL https://www.sciencedirect.com/science/article/pii/S002076831630138X.

Ebeida, M., Mitchell, S.A., Patney, A., Davidson, A.A., Owens, J.D., 2012. A simple algorithm for maximal Poisson-disk sampling in high dimensions. In: Computer Graphics Forum, vol. 31, (no. 2pt4), pp. 785–794. http://dx.doi.org/10.1111/j.1467-8659.2012.03059.x.

Falco, S., Siegkas, P., Barbieri, E., Petrinic, N., 2014. A new method for the generation of arbitrarily shaped 3D random polycrystalline domains. Comput. Mech. 54, 1447–1460. http://dx.doi.org/10.1007/s00466-014-1068-3.

Feder, J., 1980. Random sequential adsorption. J. Theoret. Biol. (ISSN: 0022-5193) 87 (2), 237–254. http://dx.doi.org/10.1016/0022-5193(80)90358-6, URL https://www.sciencedirect.com/science/article/pii/0022519380903586.

François, B., Gremeret, R., 1968. Perfectionnements apportés aux procédés pour la préparation de céramiques de matériaux tels, notamment, que les matériaux fissiles. Brev. FR1535470 (A).

Gaiselmann, G., Neumann, M., Schmidt, V., Pecho, O., Hocker, T., Holzer, L., 2014. Quantitative relationships between microstructure and effective transport properties based on virtual materials testing. AIChE J. 60 (6), 1983–1999. http://dx.doi.org/10.1002/aic.14416, URL https://aiche.onlinelibrary.wiley.com/doi/abs/10.1002/aic.14416.

Gasnier, J.B., Willot, F., Trumel, H., Jeulin, D., Besson, J., 2018a. Thermoelastic properties of microcracked polycrystals. Part I: Adequacy of Fourier-based methods for cracked elastic bodies. Int. J. Solids Struct. (ISSN: 0020-7683) 155, 248–256. http://dx.doi.org/10.1016/j.ijsolstr.2018.07.024, URL https://www.sciencedirect.com/science/article/pii/S002076831830307X.

Gasnier, J.B., Willot, F., Trumel, H., Jeulin, D., Biessy, M., 2018b. Thermoelastic properties of microcracked polycrystals. Part II: The case of jointed polycrystalline TATB. Int. J. Solids Struct. (ISSN: 0020-7683) 155, 257–274. http://dx.doi.org/10.1016/j.ijsolstr.2018.07.025, URL https://www.sciencedirect.com/science/article/pii/S0020768318303081.

Gloria, A., 2011. Reduction of the resonance error. Part 1: Approximation of homogenized coefficients. Math. Models Methods Appl. Sci. 21 (8), 1601–1630. http://dx.doi.org/10.1142/S0218202511005507, URL https://hal.inria.fr/inria-00457159.

Hill, R., 1963. Elastic properties of reinforced solids: Some theoretical principles. J. Mech. Phys. Solids (ISSN: 0022-5096) 11 (5), 357–372. http://dx.doi.org/10.1016/0022-5096(63)90036-X, URL https://www.sciencedirect.com/science/article/pii/002250966390036X.

Hsu, T., Epting, W., Kim, H., Abernathy, H., Hackett, G., Rollett, A., Salvador, P., Holm, E., 2021. Microstructure generation via generative adversarial network for heterogeneous, topologically complex 3D materials. J. Miner., Met. Mater. Soc. 73, 90–102. http://dx.doi.org/10.1007/s11837-020-04484-y.

Jeulin, D., 2000. Random texture models for material structures. Stat. Comput. 10, 121–132. http://dx.doi.org/10.1023/A:1008942325749.

Johnson, W., Mehl, R., 1939. Reaction kinetics in processes of nucleation and growth. Trans. Metall. Soc. AIME 135, 416–442.

Kanit, T., Forest, S., Galliet, I., Mounoury, V., Jeulin, D., 2003. Determination of the size of the representative volume element for random composites: Statistical and numerical approach. Int. J. Solids Struct. (ISSN: 0020-7683) 40 (13), 3647–3679. http://dx.doi.org/10.1016/S0020-7683(03)00143-4, URL https://www.sciencedirect.com/science/article/pii/S0020768303001434.

Lantuejoul, C., Maisonneuve, F., 1984. Geodesic methods in quantitative image analysis. Pattern Recognit. (ISSN: 0031-3203) 17 (2), 177–187. http://dx.doi.org/10.1016/0031-3203(84)90057-8, URL https://www.sciencedirect.com/science/article/pii/0031320384900578.

Legland, D., Arganda-Carreras, I., Andrey, P., 2016. MorphoLibJ: Integrated library and plugins for mathematical morphology with ImageJ, vol. 32, no. 22. pp. 3532–3534. http://dx.doi.org/10.1093/bioinformatics/btw413.

Makai, E., 1973. On the geodesic diameter of convex surfaces. Period. Math. Hung. 4 (2-3), 157–161. http://dx.doi.org/10.1007/BF02276103.

Matheron, G., 1967. Eléments Pour Une Théorie Des Milieux Poreux. Masson, Paris.

Meynard, J., 2019. Influence de la taille, de la morphologie et de la distribution spatiale des pores sur la conductivité thermique de céramiques UO_2. Manuscrit de Thèse.

Meynard, J., Ibrahim, M., Monnier, A., Bornert, M., Castelier, E., Duguay, C., Garajeu, M., Masson, R., 2022. Effective properties of an isotropic solid weakened by micro-cracks located at inter-granular boundaries. J. Mech. Phys. Solids 158, 104647. http://dx.doi.org/10.1016/j.jmps.2021.104647, URL https://hal.archives-ouvertes.fr/hal-03379552.

Morard, V., Decencière, E., Dokladal, P., 2011. Geodesic attributes thinnings and thickenings. In: 10th International Symposium on Mathematical Morphology and Its Application to Signal and Image Processing. ISMM 2011, Jul 2011, Verbania-Intra, Italy., pp. 200–211. http://dx.doi.org/10.1007/978-3-642-21569-8_18.

Mortazavi, B., Pereira, L.F.C., Jiang, J.-W., Rabczuk, T., 2015. Modelling heat conduction in polycrystalline hexagonal boron-nitride films. Sci. Rep. 5, 13228. http://dx.doi.org/10.1038/srep13228.

Moulinec, H., Suquet, P., 1998. A numerical method for computing the overall response of nonlinear composites with complex microstructure. Comput. Methods Appl. Mech. Engrg. (ISSN: 0045-7825) 157 (1), 69–94. http://dx.doi.org/10.1016/S0045-7825(97)00218-1, URL https://www.sciencedirect.com/science/article/pii/S0045782597002181.

Neumann, M., Stenzel, O., Willot, F., Holzer, L., Schmidt, V., 2020. Quantifying the influence of microstructure on effective conductivity and permeability: Virtual materials testing. Int. J. Solids Struct. (ISSN: 0020-7683) 184, 211–220. http://dx.doi.org/10.1016/j.ijsolstr.2019.03.028, URL https://www.sciencedirect.com/science/article/pii/S0020768319301520, Physics and Mechanics of Random Structures: From Morphology to Material Properties.

Otsu, N., 1979. A threshold selection method from gray-level histograms. IEEE Trans. Syst. Man Cybern. 9 (1), 62–66.

Pérez, I., Farias, M.M., Castro, M., Roselló, R., Morfa, C.R., Medina, L., Oñate, E., 2019. Modeling poylcrystalline materials with elongated grains. Numer. Methods Eng. 118 (3), 121–131. http://dx.doi.org/10.1002/nme.6004.

Pinot, P., 2015. Détermination de la porosité de roches calcaires : Méthode et incertitude de mesure. Rev. Française de Métrol. 2015-1 (37), 37–53.

Powell, M.J.D, 1964. An efficient method for finding the minimum of a function of several variables without calculating derivatives. Comput. J. 7, 155–162.

Remy, E., Picart, S., Delahaye, T., Jobelin, I., Dugne, O., Bisel, I., Blanchart, P., Ayral, A., 2014. Fabrication of uranium dioxide ceramic pellets with controlled porosity from oxide microspheres. J. Nucl. Mater. (ISSN: 0022-3115) 448 (1), 80–86. http://dx.doi.org/10.1016/j.jnucmat.2014.01.017, URL https://www.sciencedirect.com/science/article/pii/S0022311514000282.

Salvo, L., Cloetens, P., Maire, E., Zabler, S., Blandin, J.J., Buffière, J.Y., Ludwig, W., Boller, E., Bellet, D., Josserond, C., 2003. X-ray micro-tomography an attractive characterisation technique in materials science. Nucl. Instrum. Methods Phys. Res. B (ISSN: 0168-583X) 200, 273–286. http://dx.doi.org/10.1016/S0168-583X(02)01689-0, URL https://www.sciencedirect.com/science/article/pii/S0168583X02016890. Proceedings of the E-MRS 2002 Symposium I on Synchrotron Radiation and Materials Science.

Schindelin, J., Arganda-Carreras, I., Frise, E., 2012. Fiji: An open-source platform for biological-image analysis. Nat. Methods 9, 676–682. http://dx.doi.org/10.1038/nmeth.2019, URL https://www.nature.com/articles/nmeth.2019.

Serra, J., 1982. Image Analysis and Mathematical Morphology, Vol. 1. Academic Press.

Sevostianov, I., Kachanov, M., 2019. On the effective properties of polycrystals with intergranular cracks. Int. J. Solids Struct. 156, 243–250.

Thompson, A.W., 1972. Calculation of true volume grain diameter. Metallography (ISSN: 0026-0800) 5 (4), 366–369. http://dx.doi.org/10.1016/0026-0800(72)90018-3, URL https://www.sciencedirect.com/science/article/pii/0026080072900183.

Torquato, S., Haslach, Jr., H.W., 2002. Random heterogeneous materials: Microstructure and macroscopic properties. Appl. Mech. Rev. (ISSN: 0003-6900) 55 (4), B62–B63. http://dx.doi.org/10.1115/1.1483342.

Torquato, S., Uche, O.U., Stillinger, F.H., 2006. Random sequential addition of hard spheres in high Euclidean dimensions. Phys. Rev. E74 (6), http://dx.doi.org/10.1103/PhysRevE.74.061308.

Virtanen, P., et al., 2008. SciPy 1.0: Fundamental algorithms for scientific computing in Python. Nat. Methods 17, 261–272. http://dx.doi.org/10.1038/s41592-019-0686-2.

Willot, F., Abdallah, B., Pellegrini, Y.P., 2014. Fourier-based schemes with modified green operator for computing the electrical response of heterogeneous media with accurate local fields. Int. J. Numer. Methods Eng., Wiley 98, 518–533. http://dx.doi.org/10.1002/nme.4641.

Zhang, G., Torquato, S., 2013. Precise algorithm to generate random sequential addition of hard hyperspheres at saturation. Phys. Rev. E88 http://dx.doi.org/10.1103/PhysRevE.88.053312.